DYNAMICAL ANALYSIS OF THE FIBER OPTIC COILS THROUGH MULTISCALE NUMERICAL MODELING AND MODAL TESTS

A THESIS SUBMITTED TO
THE GRADUATE SCHOOL OF NATURAL AND APPLIED SCIENCES
OF
MIDDLE EAST TECHNICAL UNIVERSITY

BY

ÖZKAN KAHVECİ

IN PARTIAL FULFILLMENT OF THE REQUIREMENTS
FOR
THE DEGREE OF MASTER OF SCIENCE
IN
AEROSPACE ENGINEERING

APRIL 2022

Approval of the thesis:

DYNAMICAL ANALYSIS OF THE FIBER OPTIC COILS THROUGH MULTISCALE NUMERICAL MODELING AND MODAL TESTS

submitted by **ÖZKAN KAHVECİ** in partial fulfillment of the requirements for the degree of **Master of Science** in **Aerospace Engineering, Middle East Technical University** by,

Prof. Dr. Halil Kalıpçılar
Dean, Graduate School of **Natural and Applied Sciences**

Prof. Dr. Serkan Özgen
Head of the Department, **Aerospace Engineering**

Assoc. Prof. Dr. Tuncay Yalçınkaya
Supervisor, **Aerospace Engineering, METU**

Examining Committee Members:

Prof. Dr. Demirkan Çöker
Aerospace Engineering, METU

Assoc. Prof. Dr. Tuncay Yalçınkaya
Aerospace Engineering, METU

Assoc. Prof. Dr. Ercan Gürses
Aerospace Engineering, METU

Assoc. Prof. Dr. Cihan Tekoğlu
Mechanical Engineering, TOBB ETU

Assoc. Prof. Dr. Hüsnü Dal
Mechanical Engineering, METU

Date: 28.04.2022

I hereby declare that all information in this document has been obtained and presented in accordance with academic rules and ethical conduct. I also declare that, as required by these rules and conduct, I have fully cited and referenced all material and results that are not original to this work.

Name Last name : Özkan Kahveci

Signature :

ABSTRACT

DYNAMICAL ANALYSIS OF THE FIBER OPTIC COILS THROUGH MULTISCALE NUMERICAL MODELING AND MODAL TESTS

Kahveci, Özkan
Master of Science, Aerospace Engineering
Supervisor: Assoc. Prof. Dr. Tuncay Yalçınkaya

April 2022, 82 pages

Fiber optic gyroscopes (FOGs) are common rotation measurement devices in aerospace applications. They have a wide range of diversity in length and winding radius of coils to meet the system requirements. Every dimensional parameter in the coil influences the dynamic response of the system, which eventually leads to measurement errors. In order to eliminate the errors and qualify the system, after the design and production stages, a deep and comprehensive testing procedure follows. In this study, the dynamic behavior of a quadrupole winded fiber optic coil is investigated. Firstly, a set of fiber optic coils are tested with an impact modal test, where mode shapes and natural frequencies are determined with structural data acquisition. For the modal analysis, a finite element (FE) model is developed where a representative volume element (RVE) analysis is also included to consider the influence of the microstructure properly. The experimental and numerical results are compared and validated. Moreover, an estimation model is proposed for a type of coil with different fiber length. Finally, the latter coil set is produced and tested employing the same methodology in order to illustrate the capacity of the developed framework.

Keywords: Fiber optic gyroscope, Fiber optic coil, Modal test, Modal analysis, Finite element method.

ÖZ

FİBER OPTİK BOBİNLERİN ÇOK ÖLÇEKLİ SAYISAL MODELLEME VE MODAL TESTLERLE DİNAMİK ANALİZİ

Kahveci, Özkan
Yüksek Lisans, Havacılık ve Uzay Mühendisliği
Tez Yöneticisi: Doç. Dr. Tuncay Yalçınkaya

Nisan 2022, 82 sayfa

Fiber optik jiroskoplar (FOJ'lar), havacılık uygulamalarında yaygın olarak kullanılan rotasyon ölçüm cihazlarıdır. Sistem gereksinimlerini karşılamak için bobinlerin uzunluk ve sarım yarıçapı bakımından geniş bir çeşitlilik yelpazesine sahiptirler. Bobin içindeki her boyutsal parametre, sistemin dinamik tepkisini etkiler ve bu da nihayetinde ölçüm hatalarına yol açar. Tasarım ve üretim aşamalarından sonra hataları ortadan kaldırmak ve sistemi kalifiye etmek için uzun ve kapsamlı bir test prosedürü izlenir. Bu çalışmada, bu uzun prosedürü ortadan kaldırmak için “quadrupole” sargılı bir fiber optik bobinin dinamik davranışı incelenmiştir. İlk olarak, üretilmiş fiber optik bobinler, mod şekillerinin ve doğal frekansların yapısal veri toplama ile belirlendiği bir darbe modal testi ile test edilmiştir. Modal analiz için, mikro yapının etkisini uygun şekilde değerlendirmek amacıyla temsili hacim elemanı (THE) analizinin de dahil edildiği bir sonlu eleman (SE) modeli geliştirilmiştir. Deneysel ve sayısal sonuçlar karşılaştırılmış ve doğrulanmıştır. Ayrıca, farklı fiber uzunluğuna sahip başka bir bobin tipi için bir tahmin modeli önerilmiştir. Son olarak, geliştirilen çerçevenin kapasitesini göstermek için aynı metodoloji kullanılarak bu bobin seti üretilmiş ve test edilmiştir.

Anahtar Kelimeler: Fiber optik jiroskop, Fiber optik bobin, Modal test, Modal analiz, Sonlu elemanlar yöntemi.

To my family.

ACKNOWLEDGMENTS

Firstly, I would like to express my genuine gratitude to my thesis supervisor Assoc. Prof. Dr. Tuncay Yalçınkaya for his guidance throughout my thesis study. His positive attitude and faith made me stand firm.

Then, I wish to express my sincere thanks to my manager Caner Gençoğlu for their advices and encouragements throughout the research.

I would like to thank my colleagues Hasan Yetgin, Hasan Baran Özmen, Denizhan Yerel, Tevfik Ozan Fenercioğlu and Yasin Cihaner for their support and motivation to climb this greasy pole.

Also, I would like to thank my company Roketsan Missiles Incorporation for making this work possible.

Finally, I would like to express my sincere thanks to my mother Fatma, my father Selahattin and my sister Özlem for their endless support and love.

Lastly, I am grateful to my wife Sevde Bengisu Kahveci for her beloved support and faith during this work.

TABLE OF CONTENTS

CHAPTERS

LIST OF TABLES

TABLES

LIST OF FIGURES

FIGURES

LIST OF ABBREVIATIONS

ABBREVIATIONS

ARW : Angular Random Walk
CVG : Coriolis Vibratory Gyroscope
EMA : Experimental Modal Analysis
FOG : Fiber Optic Gyroscope
FEA : Finite Element Analysis
FEM : Finite Element Method
FFT : Fast Fourier Transform
FRF : Frequency Response Function
LMS : Leuven Measurement System
MEMS : Micro-Electro-Mechanical Systems
MTR : Modal Test Robot
PM : Polarization Maintaining
RLG : Ring Laser Gyroscope
RVE : Representative Volume Element
SAP : Stress Applying Part
VRE : Vibration Rectification Error

LIST OF SYMBOLS

SYMBOLS

E : Elasticity Modulus [N/m^2]

G : Shear Modulus [N/m^2]

σ : Stress Tensor [N/m^2]

ε : Strain Tensor [N/m^2]

S : Elastic Compliance [m^2s/N]

n : Refractive Index

CHAPTER 1

INTRODUCTION

In recent years, the technology of guidance and control of the system is becoming very crucial due to the needs of rotation, acceleration, position and precession motion information of the platforms. Research and explorations into the physical theory and structural behavior of a system are propelling rapid advancements in navigation technology. Improving our understanding of the causes and solutions of system faults, as well as the theoretical relationships between concepts and observations not only in the actual world but also in the virtual world, leads to new and advanced future technological breakthroughs.

The trajectory and velocity of a vehicle are calculated by using mathematical integration of acceleration and angular rate measurements while considering the original orientation and position. Gyroscopes are sensors that detect the rotation rate using several principles of operation techniques. There are numerous architectures, design methodologies and production technologies regarding gyroscopes in the literature. Gyroscopes play a significant part in current navigation systems for arranging, diagnosing and controlling the motion of a vehicle from one location to another.

The understanding of gyroscope theory, mathematics and improvements in the accomplishment of mistakes caused by external elements such as temperature change, vibration, shock, acoustic and magnetic factors are all improving with the developing technology by the day. When it comes to optical gyroscopes, one of the most compelling failures is vibration which causes measurement errors that reduces the performance of the sensor.

1.1 Gyroscope Technologies

In a general manner, a gyroscope is a device that measures orientation and angular velocity in a rotating frame [1, 2]. Gyroscopes are widely used in aerospace industry as well as military, automotive, medicine and so on [3]. The gyroscopes can be categorized by means of their operating principles. The basic classification of the gyroscopes in terms of their fundamental architectures are presented in Figure 1.1 [3, 4, 5].

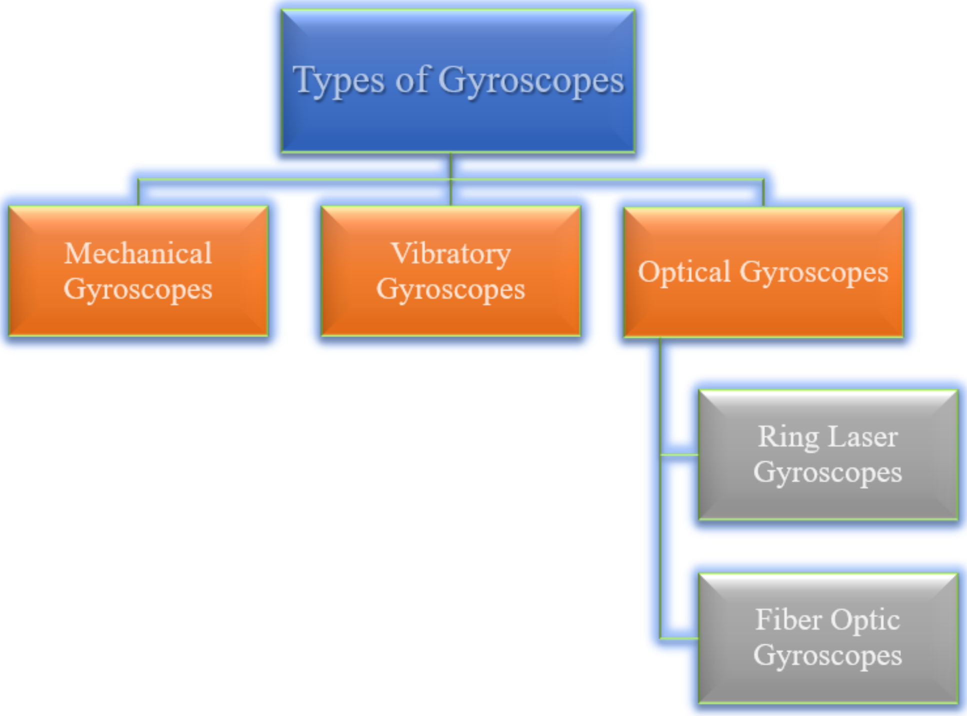

Figure 1.1 Gyroscope types

There are mainly three types of gyroscopes based on their working principles. In following subsections, the basic working phenomenon, physical principles and common application areas are explained for the gyroscopes.

1.1.1 Mechanical Gyroscopes

The mechanical gyroscopes were invented during the research to find the rotation of the Earth by Leon Foucault in the year 1982 [3]. The phenomenon of mechanical gyroscopes is the conservation of the angular momentum. Mechanical gyroscopes are also known as conventional gyroscopes at the beginning of the invention years.

The mechanical gyroscopes essentially have a spinning mass or wheel which rotates around its axis (Figure 1.2). The spinning part is supported by a pair of gimbals in each axis and freely spins at any orientation [6]. If there is an external force applied to the system in any axis or orientation, it tends to resist the motion and remain parallel to itself.

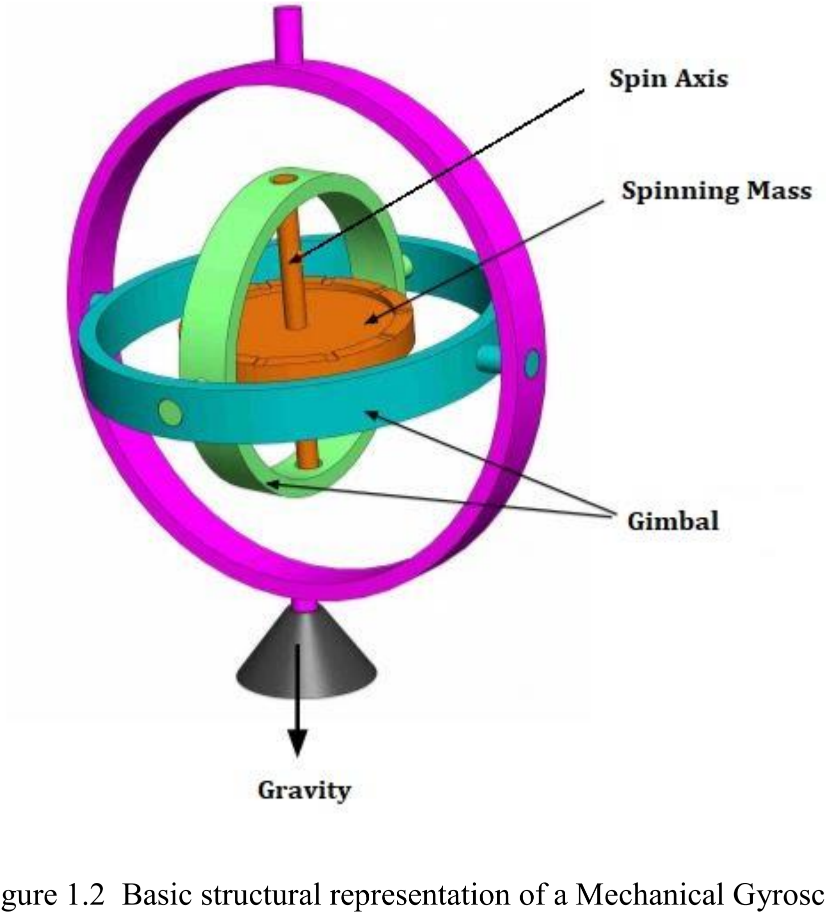

Figure 1.2 Basic structural representation of a Mechanical Gyroscope

Newly developed mechanical gyroscopes are much more compact and tinier compared to the traditional mechanical gyroscopes which were big and bulky. The biggest drawback with the mechanical gyroscope is the moving parts which result in friction during rotation. The friction reducer materials are generally hard to find or expensive.

The sensing performance of mechanical gyroscopes can be very precise especially in harsh environments. They have robust design configurations in the applications of marine environments and military applications. These configurations are named rate-integrating, spinning mass, flex, single degree of freedom and dynamically tuned gyroscopes by their field of applications [4].

1.1.2 Vibratory Gyroscopes

Vibrating gyroscopes were developed in the early 1950s and they are operated by the Coriolis Effect [6]. The Coriolis Vibratory Gyroscope (CVG) is a very good example of a vibratory gyro which uses a vibrating mass or a specifically designed structure to calculate the rate of rotation. There are many types and geometries of vibrating structures even at the micro levels.

The idea proposed by Foucault that a vibrating element in a rotational system preserves its plane of vibration has led to the concept of sensing both angular rate and linear velocity. Coriolis Effect has an inertial force of the mass which is moving with a certain velocity and rotating with an angular velocity (Figure 1.3). There are variety of vibratory gyroscope types that are simpler and cheaper than conventional rotating gyroscopes of similar accuracy. Especially in automotive and industrial robotics applications, MEMS and quartz MEMS gyros are widely used. Also, under vacuum conditions, hemispherical resonator gyroscopes (HRG) made of quartz glass are used for spacecraft orientation purposes. Vibrating wheel gyroscopes, hemispherical resonator gyroscopes, cylindrical resonator gyroscope (CRG), tuning fork gyroscopes, vibrating disc gyroscopes are common types of vibratory gyroscopes [4, 5].

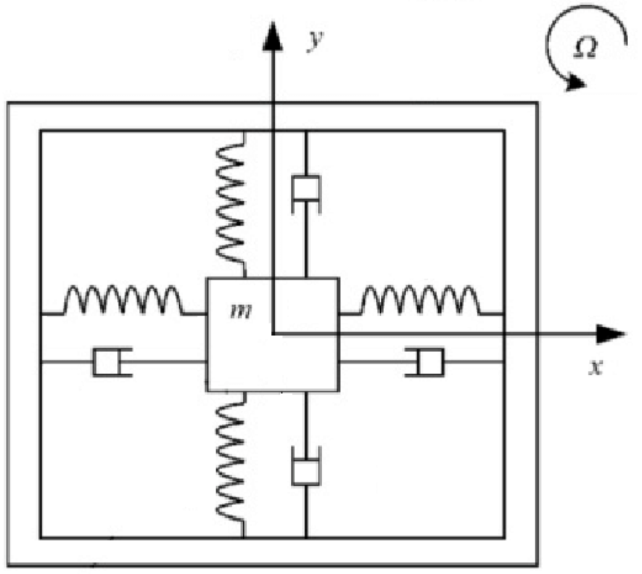

Figure 1.3 Schematic of a vibratory gyroscope

The most common and up-to-date version of the vibratory gyroscope type is called Microelectromechanical Systems (MEMS). MEMS gyroscopes are packaged like the standard integrated circuits and can give an output analog or digital depending on their application areas. They are widely used in automotive industry because of their high compactness and low costs [1, 5].

1.1.3 Optical Gyroscopes

Optical gyroscopes are different from the previously explained types of gyroscopes, simply have no moving parts. This means they do not deal with friction or inertia based problems. This is a great advantage by means of reliability compared to the traditional mechanical gyros. Nevertheless, MEMS gyroscopes are smaller and cheaper, but they do not have higher performances compared to the optical gyroscopes [5]. The optical gyroscopes work with the principle of the Sagnac effect which is explained in Section 2.1. There are two main types of optical gyroscopes that work with the Sagnac principle, Ring Laser Gyroscope and Fiber Optic Gyroscope (Figure 1.1).

1.1.3.1 Ring Laser Gyroscopes

The theory of Sagnac was proposed on the paper drafts for circular geometries like a wound fiber coil, but there is no fiber optic cable production technology at these years, so the concept is constructed to realize the theory with the mirrors which reflect the propagating lights [1]. The cross section of a Ring Laser Gyroscope is shown in Figure 1.4.

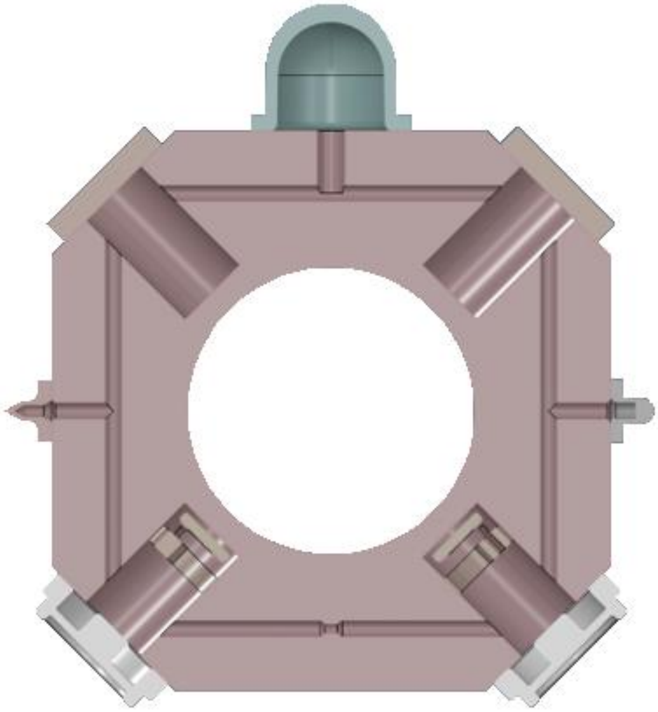

Figure 1.4 Classical representation of a Ring Laser Gyroscope

A typical one axis square frame RLG configuration contains 2 concave and 2 planar mirrors to construct the Sagnac interferometer [1,4,7]. Also, a triangular framed one axis RLG configuration exists because of the lower cost and easy manufacturing, but they are less sensitive compared to the square framed RLG configurations.

The basic problem with the RLG is the higher production costs, packaging limits and the complexity of some specific processes during the production stages. On the other hand, they can have higher precision levels compared to the other types of gyroscopes. They are widely used to meet the high precision requirements of aerospace and naval systems where the weight, size and cost limits are not strictly limited by the application area [3, 4].

1.1.3.2 Fiber Optic Gyroscopes

Fiber-optic gyroscopes (FOGs) are rotation sensing devices utilizing Sagnac's principle. They use phase difference between two counter traveling laser waves to compute the rotation motion of the body they are attached to [1,4,7]. From a laser source, two counter propagating light beams are injected into the same fiber in opposite directions. As a result of the Sagnac effect, the path of the light beam gets shorter while the other travels longer under a rotation and a phase shift occurs, as explained in detail theoretically in Section 2.1. The phase shift is measured differentially through Sagnac interferometry [1,4,7]. FOG sensors work on a similar principle to ring laser gyroscopes (RLGs); however, FOGs offer many advantages over RLGs, such as low cost, low weight, low power consumption, no precise machining requirement, no gas medium or leakage problems, and no vibratory mechanism to overcome lock-in problems at low rotation rates [8,9]. In recent decades, FOG technology has developed rapidly owing to advances in low-loss fiber-optic cables, light sources, and detectors used in the telecommunications industry [1,8,10]. A FOG sensor is mainly composed of a light source, a coupler, a phase modulator, a photo detector, and most essentially, a coil of fiber-optic cable [7,11–14].

The necessary and sufficient components to construct the most basic FOG sensor structure are given with a simple schematic in Figure 1.5. In this schematic, there is a broadband light source providing small coherence to eliminate the errors coming from optical non-linearities [3].

A Photodiode senses the optical power of the system. The power is then transduced to the electrical power. The common types of photodiodes are PINFET types due to the power efficiency and quantum efficiency levels with the help of the recent developing technology [1,15].

Couplers are the components that are used to split the light or recombine the travelling light beams in the system. So, two light beams can be divided into different paths and the light beams coming from different paths can be directed in one path. There are different kinds of couplers used in industry according to desired type provided that the reciprocal configuration is suitable [1,15].

The optoelectronic component that is composed of Lithium base Y junction waveguide is called MIOC in a FOG structure. MIOC is a phase modulator which creates the response into the closed loop feedback signal of the system [15]. MIOC can also perform as a polarizer and influences the FOG accuracy. The light power is divided into half of the original power intensity and directed to two different paths of the fiber coil [1].

Reciprocity is a term that shows basically how symmetric the system is. In a reciprocal system, the two light beams propagating in counter directions travel exactly the same path [1]. Thus, they should travel in phase when the system has no rotation. If there is a phase shift at rest, there is a power imbalance between light beams [11].

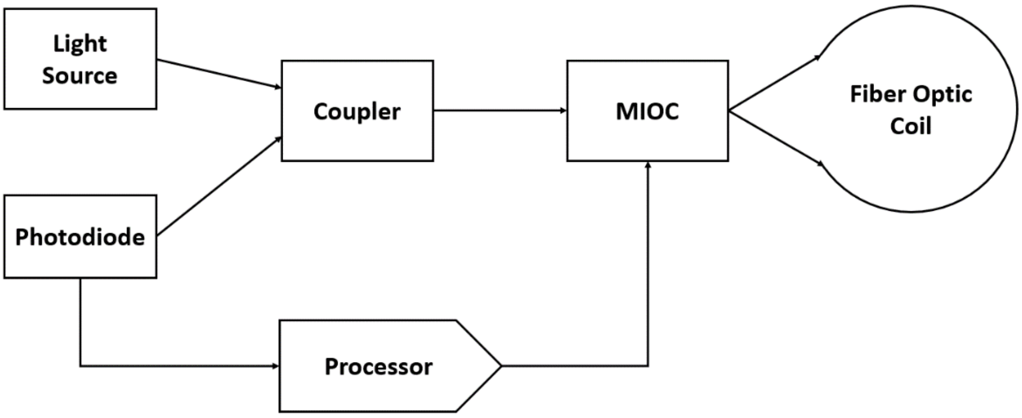

Figure 1.5 Schematic of a simplest FOG sensor structure

A FOG can provide a wide range of sensitivity based on the total length of the winded fiber which can vary from even a hundred meters up to 5 kilometers depending on the required precision and the needs of the platform.

In order to ensure the precision of a FOG sensor, maintaining the symmetrical loading for the clockwise and counterclockwise paths along which light travels is crucial for the performance. Due to the effects of thermal and mechanical stresses on a FOG coil, the refractive index of light differs in the fiber-optic cable causing an unsymmetrical loading difference between the clockwise and counterclockwise paths that light travels along, eventually resulting in a bias error at the sensor readout [1,14].

In case of a time-dependent temperature gradient occuring along the fiber, non-reciprocity bias errors known as the Shupe effect arise [16]. As a solution to this problem, symmetric coil-winding methods are suggested [17]. A commonly preferred method is the “quadrupole” winding pattern, yet other novel patterns and methods to overcome non-reciprocity errors are being studied in the literature [18–20]. The errors due to temperature effects in a FOG sensor are able to be analytically modeled, and these errors can be compensated from the sensor output by employing proper algorithms [21–25]. The utilization of the finite element (FE) method is an alternative approach to the analytical modeling of disturbance effects due to temperature variations on FOG coils [26–30].

There is a fiber optic coil which is called Coil Type-1 in this study. Based on existing gyro parameters of Coil Type-1, a research study started to develop a different grade product with a shorter required total fiber length, which is named in this document as Coil Type-2 (Figure 3.14) and have approximately half of the total fiber length of Coil Type-1 (Figure 3.13). At this stage, the vibrational characteristics of the developing fiber-optic gyroscope need to be studied. The workflow of the study begins with creating the RVE model for the composite coil structure, which consists of the fiber, the coating layer of the fiber, and the adhesive applied between the fibers. The material properties are taken from the supplier datasets and the RVE parameters are then calculated in the sequence, as explained in Section 3.2. After the modal tests for the Type-1 coil batch, the global FE model is created and the results are compared with the test results. The RVE parameters and the global cylindrical FE model are set, and from the global model of the Type-1 coil, the global model for the Coil Type-2 is established and the dynamic properties of the Type-2 coils are estimated. Later, the Type-2 coil batch is produced and the same modal test procedure is applied. The cylindrical global FE model for the coil structure uses the verified RVE parameters as input and the geometric features as parameterized properties to give the designer the freedom to decide on further design configurations based on the changing fiber length by using the dynamic response of the coil. By fitting the FE model, the designer can decide on the geometric properties and materials that the coil support configuration should have for new coil structures.

1.2 Motivation and Scope of the Thesis

The aim of this study is to construct a baseline study for the robust coil support designs against vibration problems for a FOG sensor. The coil can be considered as a composite structure due to its nature. In order to accomplish a FE study on the coil and coil support assembly, one should simulate the behavior of the coil part by considering the microstructural effects of the fiber materials as well as the adhesive parts. After finding the global material properties of this composite coil by starting from the microstructure, one can simulate the dynamic behavior of the global coil by using FEA. Thanks to the FE methodology, the designer can detect the natural frequencies and the mode shapes of the structure. The vibrational information of the structure is then used to decide on the raw material and the geometry of the coil support to enhance the sensing performance for the assembly of the FOG sensor. By using such FE methodology to design a superior sensor by means of vibration characteristics, the production costs can be reduced or totally avoided and the testing stages of the fiber optic coil can be estimated in the development of the sensor before the qualification processes.

The thesis is organized as follows. First, in Section 2, the literature review conducted for the study is presented. In Section 3 of the thesis, the material properties of fiber, adhesive, and coating are presented. In addition, the utilized computational framework of the RVE parameters by using finite element method theory and the modal test methodology applied for the fiber optic coils are explained. Next, the global FE analysis results and the modal test results for both coil configurations are discussed in Section 4. Finally, the discussion and the conclusion of the work are presented in Section 5.

CHAPTER 2

LITERATURE REVIEW

In order to achieve better design solutions, a detailed literature survey is conducted. In chapter 2.1, performance of FOG sensors are explained.

2.1 Sagnac Effect

The French physicist George Sagnac discovered that the angular rate can be detected by using an interferometric device in 1913[1]. When the system rotates, two light beams which travels on the same fiber in opposite direction create an interference due to the phase difference (Figure 2.1). The interference occurred is proportional to the rotation amount of the system, so the system rotations can be measured.

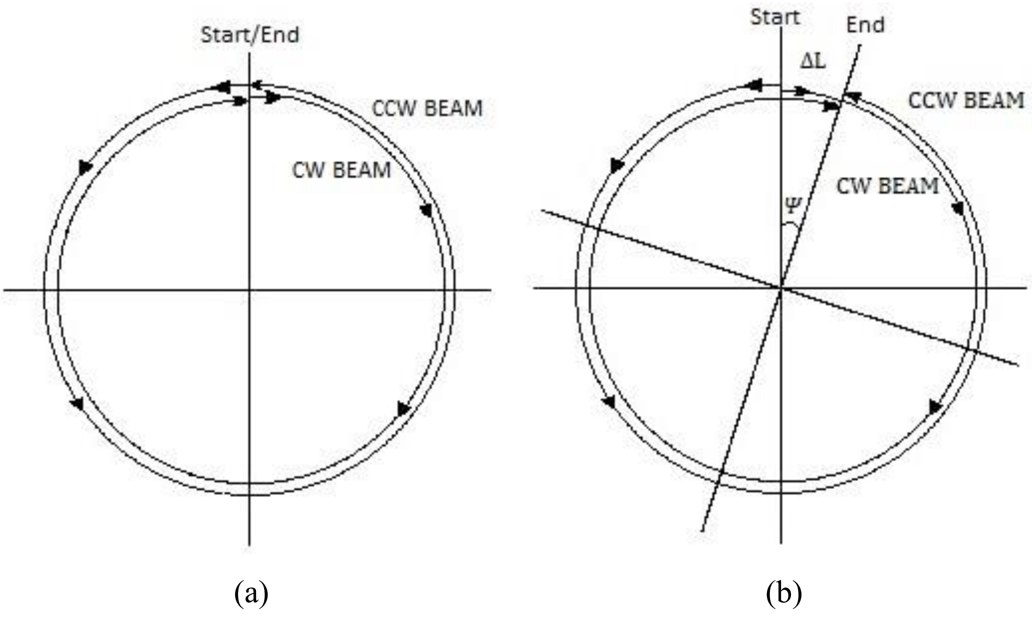

(a) (b)

Figure 2.1 No rotation light waves (a) and under rotation Ψ light waves (b)

In this configuration, after a small amount of time, the light beams arrive at the point where they started with the exact same time. They have the same velocity and the distance between the start and end points. In situation (b), the system is under a rotation with an angular velocity of Ψ, so the CCW beams travel less distance compared to the CW beams as a result of rotation [7]. This situation causes a phase shift between the CW and CCW light waves, so the angular rate can be determined mathematically from this proportional phase shift by using the radius of the coil and the length ΔL (Figure 2.1).

2.2 Shupe Effect

Thermal differences on a FOG sensor affect the sensing characteristics of the coil structure and causes bias error. In FOGs, the temperature transience error is known as the Shupe effect. This effect and its relation to temperature-induced stresses are critical occurrences of FOG technology in a coil structure [1].

In a FOG, the light propagates in the core of the fiber and some integrated optic components. As a consequence of the physical properties of the fiber material, the Kerr effect and the Shupe effect are encountered as parasitic deteriorations in the optical components and light itself acting as birefringence, backscattering and back reflections [1, 16].

The light beams traveling in its waveguide which is the core of the fiber will propagate in different paths if the refractive index changes depending on changing temperature conditions. This means that the CW and CCW light beams interfere with a delay at the output and travel in dissimilar modes. As a result of thermal distortions, the birefringence in fiber changes and causes unwanted phase shifts [4, 31]. These phase shifts then contribute to bias, bias instability and angular random walk (ARW) of a FOG [1]. In addition, these thermal changes affect the thickness and the length of the coil which produces scale-factor changes in the gyroscope [4].

In order to reduce the Shupe effect on a FOG coil, the fibers are winded as symmetrical structures [1]. The symmetrical windings may have a pattern as multiple of 2 or multiple of 4 around coil axis and they are called dipolar winding types. In a dipolar winding scheme, the radial heat propagates through the same half-coil length with a pair of symmetrical layers and it causes a residual sensitivity in for a transient time by the propagating heat.

There is a common winding method used to reduce these types of temperature errors called as quadrupole winding method. In a quadrupolar winding, the layer order is reversed from pair to pair and this reversed order neutralizes the temperature effect and improves the compensation by the winding direction (Figure 2.2).

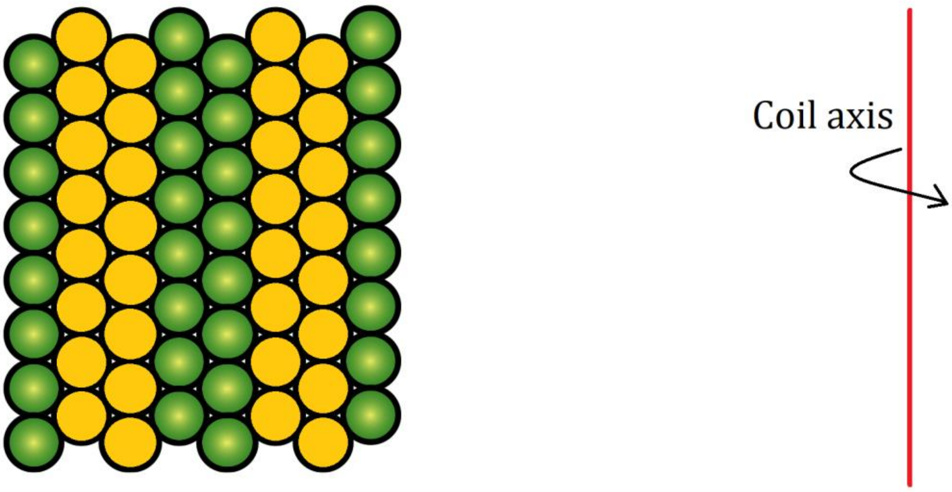

Figure 2.2 Schematic of a quadrupolar winding configuration

In Figure 2.2, the red line represents the centerline of the coil. The fibers are arranged as multiples of 4 lines and wound in opposite directions. The green fibers are wound in clockwise direction while the orange ones wound in counter-clockwise direction. The total fiber length of the coil should be decided by considering the layer count as the multiples of 4 or a complete quadrupole to maintain the symmetry of the structure in order to reduce the Shupe effect.

2.3 Vibration Problems of FOG Sensor

Mechanical loadings are as important as thermal loadings on the performance of FOG sensors. The success of a FOG sensor is related to low stress levels on the fiber-optic cable wound on the coil. There are studies in the literature that focus on addressing methods for reducing stress on FOG coils during the winding process [12,32,33]. Other than winding processes, one source of stress in FOG coils is mechanical vibrations. Modeling and compensating the effects of mechanical vibrations has been the subject of certain studies [34–36]. In order to reduce the vibration-based errors and identify the characteristics of the system, the FE theory has also been used to determine the resonance frequency of the structure to enhance the performance of FOGs [37,38]. FE modeling of the mechanics of rotations sensors is also utilized for RLG sensors as well as FOG sensors [39]. Thanks to FE methodology, deflections and stress distributions on the sensitive parts of optical sensors working with the Sagnac principle can be computed accurately [40,41].

In order to have a rugged FOG design configuration with high reliability and good ability to resist the shock and vibration loadings, there are many ways to improve the dynamic performance of FOG sensors. Robust designs of FOG sensor bring many advantages in the sensing performance. However, the advantages can be detected only after a series of measurements and tests over the system [31]. The deterioration in the FOG performance is caused by the parameter variations is the crucial cause that leads to the vibration error in low frequency range. Thus, it is essential to fix the fiber optic coil with a robust mechanical design [31].

During the operation of the sensor, the error coming from the resonance frequency of the structure is much larger than the other frequency values. In the design stage of the mechanical structure of a FOG sensor, resonance frequencies should be avoided within the working frequency range. In aerospace applications, the operating range in frequencies should be less than 2 kHz. Therefore, the assembly method of the FOG coil and the attached mechanical geometry should be designed to avoid such resonance frequencies in this range. The design of the mechanical structure has a high impact on the vibration error levels of a FOG [37,40,41].

The vibration performance of the sensor and the resonance frequencies can be simulated through FEA. In order to see the vibration spectrum and frequency response of the system, such testing methods are available based on the assembly level by means of mechanical or optical readouts of the sensor.

2.3.1 Vibration Rectification Error for FOG

Vibration rectification error (VRE) is a term generally used for accelerometer output stability. When an accelerometer converts alternating current vibration patterns to direct current patterns, or rectifies, VRE occurs. This rectification is a result of non linearities and asymmetries in the sensor and produces errors.

In FOG, the similar term used to define vibration based error of FOG is called as bias instability and it is defined as the drift that the measurement has from its average value of the output rate. The bias stability can be measured and it shows that how stable the gyro output is over a certain period over time. This stability can be disturbed from such effects, mostly on thermal and vibration based amplifications throughout the lifecycle of the gyroscope.

The long term average of the data is collected from a long sequence of data and the average value is found which is bias. Bias stability is the change in the bias measurement over a time period. In order to have a stable bias value, the mechanical and opthomechanical design should be robust against vibrational loadings [42, 43].

2.3.2 Finite Element Analysis of FOG

In the finite element analysis (FEA) of FOG coil conducted here, a meaningful section of the coil, including a single fiber with a fiber core, cladding, glue, and sections of neighboring cables, is modeled in an appropriate symmetry boundary condition to represent the global behavior of the coil material. This section is called the representative volume element (RVE) and a homogenization procedure is followed where the coil material properties are obtained from the RVE [26,28,29,31,44,45,46,47]. FOG coil is composed of a fiber-optic cable in a staggered formation glued to each other by adhesives in an orderly fashion. The fiber-optic cable is composed of a fiber core in which light travels and the fiber core is covered by protective cladding [11,12,24,27,48,49]. Since the coil structure is composite, the methods of homogenization for modeling the mechanical and thermal properties of composite structures also hold for the FOG coil, and in this study, such an approach is followed [50–57].

The studies that include an FEA of FOG coils mostly tackle thermal loading problems; however, a study in which the mechanical modeling of a FOG coil with the FE and RVE methods and the results verified using vibration testing is rare. In the literature, the computation of the orthotropic elastic properties of composite structures utilizing impact hammer modal testing and FE analysis has been addressed [58]. In this study, the mechanical characterization of a FOG coil has been extracted by employing the RVE approach using FEA. With proper material properties, the RVE model of the FOG coil is established. Through the RVE model, obtained homogenized orthotropic elastic properties are used in a solid FOG coil FE model to calculate the natural frequencies and mode shapes of the coil. These vibrational properties of the FOG coil from the FEA are verified by the data obtained through impact hammer modal testing. For the modal testing, the coil structure is suspended using soft elastic rubbers to make free boundary conditions, the smallest possible accelerometers have been used to reduce the mass coupling effect, and the excitation is generated by an impact hammer attached to the automated modal test robot (MTR) in order not to make the coupling between the FOG coil and the exciter [59,60]. Moreover, an estimation model is proposed and tested against other coils with different dimensions. A different coil type is produced and tested, and the estimation of the FE model is verified by testing the new coil batch. It is important to point out that the verification of the homogenized material properties of FOG coils by means of impact modal testing is a novelty for the literature. In order to accomplish this, a scientific approach has been developed for a practical engineering problem. Thanks to this method, researchers have the opportunity to assess the dynamic behavior of a newly designed FOG coil prior to cumbersome testing processes. This complete multiscale modeling with experimental verification is a unique study for the literature.

FOG coil has been modeled to be perfectly symmetric, and with such structures, double modes are expected at the same frequency as two orthogonal mode shapes [61]. Due to the nature of the quadrupole winding method, the jogging zone causes these twin modes to occur slightly separated, with the nodal lines of these modes being fixed. Using modal testing and a finite element analysis approach, a FOG model with verified orthotropic elastic properties is obtained.

The material matrix of three dimensional RVE of the fiber optic coil is modeled with the finite element method (FEM). An ABAQUS script for homogenization of material properties uses volume average of stresses in the RVE. Homogenization of composite structure is performed by linking the RVE script and global model script in ABAQUS software. Calculated elastic properties of the homogenized material are used as an input to the global coil model.

The procedure applied to simulate the dynamic behavior of a FOG coil by using FE method is explained in detail in Section 3.2 of the thesis.

CHAPTER 3

METHODOLOGY

In this study, a FEM is established by using an RVE approach in order to obtain the equivalent homogenized material properties of a fiber-optic coil wound by a quadrupole winding method. In order to establish the mechanical model, the material behavior needs to be identified. In this chapter, the materials of the coil, the production stages of the coils and the produced coil configurations for this study are introduced in Section 3.1. In Section 3.2, the RVE methodology followed to solve the FE model of the coil is explained theoretically. In Section 3.3, the modal test methodology and the applied testing procedure to the produced coil configurations are expressed.

3.1 Materials

The materials of a FOG coil can be divided into two main categories as fiber and adhesive (Figure 3.1). Generally, fiber consists of three layers as core, cladding and a coating part. Fiber is generally wound onto a mandrel disk with a winding machine by utilizing a well-known winding method among the literature. At the same time, an adhesive is applied between the fibers layer by layer all through the winding process. When the winding process is completed, the coil and the winding mandrel is exposed to a two-stage curing procedure to complete the curing process of the adhesive. Then the complete structure is kept under low temperature to remove the coil from the winding mandrel with the help of the thermal expansion difference between the winding mandrel and the coil. After that, the removed free stand coil is assembled to the coil support structure together with the other optical and electronical equipment and mounted to the sensor mount platform.

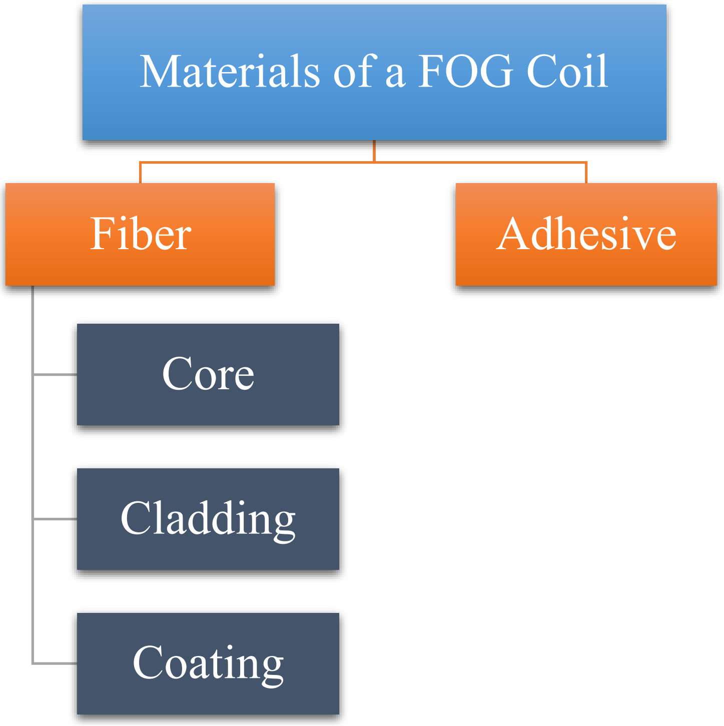

Figure 3.1 Fundamental materials of a FOG Coil Structure [62]

There is a core and a cladding layer in an optical fiber structure. The light is guided in the core region which can be produced from a wide range of glass or plastic materials. Silica based glass fibers have a lot of advantages and they have become well-established and comprehensive ones. There are various types of fibers with different internal structural features which offer excellent guidance attributes by means of birefringence with the help of stress including cladding structures.

A gyroscope fiber is a highly birefringent polarization maintaining (PM) one which is used in FOG coil production. A PM fiber maintains the polarization state of light and reduces the probability of cross coupling. These fibers offer particular mechanical and optical performance suitable for a circular winding operation. Also, the gyroscope coils may have a total fiber length up to a few kilometers depending on the application, so the fiber must be suitable for a circular winding at small diameters like a few centimeters. Furthermore, the fiber should withstand the harsh vibrational impacts and perform under wide temperature range throughout the lifecycle of the sensor.

The core is the center of an optical fiber where the light propagates (Figure 3.2). The common materials for the core region are pure silica or germanium doped silica depending on the application. The light is guided in this glass region of the fiber by the refractive index difference between the core and the cladding regions. The refractive index defines the ratio of the speed of light in the material with respect to the speed of light in vacuum conditions (Equation. 3.1). The speed is the phase velocity ϑ_p.

$$\vartheta_p = \frac{c}{n(\lambda)} \tag{3.1}$$

Equation. 3.1 shows that the phase velocity of the light in a medium is lower than the speed of the light in a vacuum condition.

Equation. 3.2 shows how the refractive index n relates the wavelength of light in the medium λ to the vacuum wavelength λ_0.

$$n(\lambda) = \frac{\lambda_0}{\lambda} \tag{3.2}$$

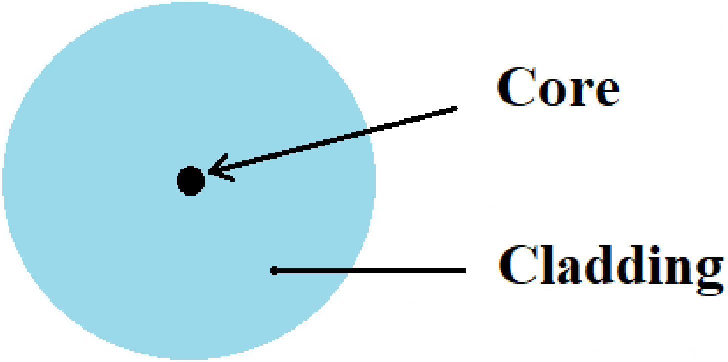

Figure 3.2 Basic fiber geometry

The cladding region of the fiber is the region surrounding the core of the fiber (Figure 3.2). The cladding is also a glass part same as the core of the fiber. In order to guide the light in the core region of the fiber, the cladding should have lower refractive index compared to the core region. With the help of the refractive index difference, the light is kept in the core without escaping to the cladding region of the fiber. The typical materials for the cladding are fluorine-silica doped glasses or low index polymers.

In some gyro fibers, the stress applying parts (SAPs) are placed in the cladding of a PM optical fiber at opposite sides of the core. The purpose of SAPs is inducing the birefringence. SAPs are made out of materials with a different thermal expansion compared to the thermal expansion coefficient of the fused silica core material which is the typical cladding material. In production stages of the fiber, while the fiber cools down, the different thermal expansion coefficient of the SAPs creates a little stress along one axis of the core. It creates a higher birefringent fiber. There are different shapes of SAPs and the two most famous polarization maintaining fibers in the optical market are Bow-Tie and Panda shapes (Figure 3.3).

The coating region is a non-glass cover of the fiber which surrounds the glass parts by offering a mechanical protection (Figure 3.3). The common material for a coating is acrylate which can withstand higher temperatures while operating gyro applications. They have Polyimide (PI), High Temperature Acrylate (HTA) or Carbon types as single or dual layers depending on the application area.

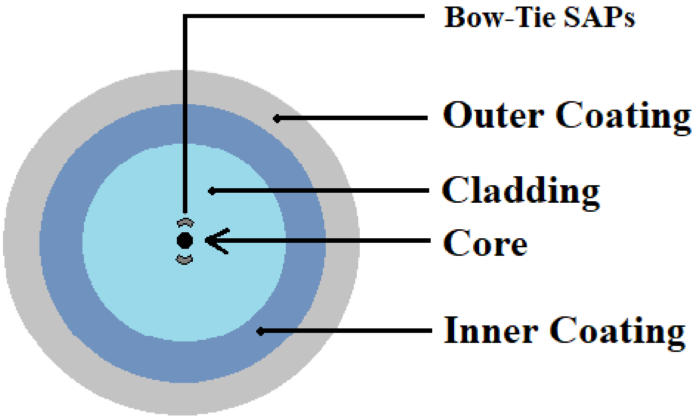

Figure 3.3 Coating geometry of a fiber

The adhesive application in the winding process is required to hold the fibers together and produce a free stand coil. In this study, Epo-Tek® 330 is chosen as the coil adhesive due to its extremely wide application in gyroscopes and in aerospace industries. It is a high-temperature grade, thermally insulating for fiber optics applications. The adhesive is a low viscosity optical epoxy which contains two components as the syringe and the adhesive itself. The syringe improves the viscosity and the effective pot life of the adhesive until the application. The components are mixed with a ratio of 10:1 by weight in a single pot and the bubbles are removed from the adhesive mixture by applying a small stirring process and a curing process in a vacuum oven. The vacuum process approximately takes 30 minutes under 50 °C to remove the aerial impurities from the adhesive mixture.

3.1.1 Specifications of the Used Fiber

Regarding fiber material, the technical specifications are given in Table 3.1. The coils are produced with the quadrupole winding method. The dimensions of the core, cladding, and coating parts are 6.5, 80, and 155 µm, respectively as shown in Figure 3.4.

Table 3.1 Technical specifications of used fiber

Parameter	**Value**
Core Diameter (µm)	6.5
Cladding Diameter (µm)	80 ± 1
Core Cladding Concentricity (µm)	≤1.0
Coating Diameter (µm)	155 ± 5
Coating Type	Dual Acrylate

The dual layer acrylate coating is considered as a one united layer due to the use of the same material as two layers. Thus, the coating part is modeled from the 80 micrometers of diameter to the 155 micrometers of diameter by means of mechanical contribution.

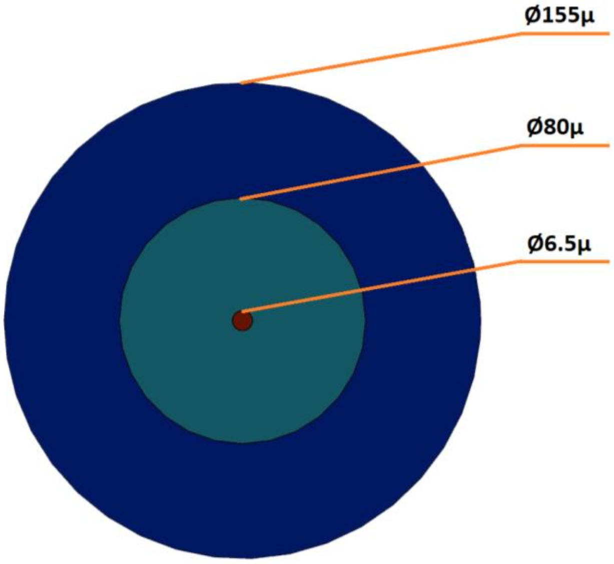

Figure 3.4 The cross-sectional view of fiber dimensions

3.1.2 Quadrupolar Winding Process of a FOG Coil Production

The winding process starts with the basic dimensioning of the coil. The inner diameter, outer diameter and height must be defined considering the available space for the coil. The winding mandrel and the limiting mandrel geometries which defines the coil dimensions together, should be suitable for the free stand coil production by taking into account the removal stage of the coil from the mandrels (Figure 3.5).

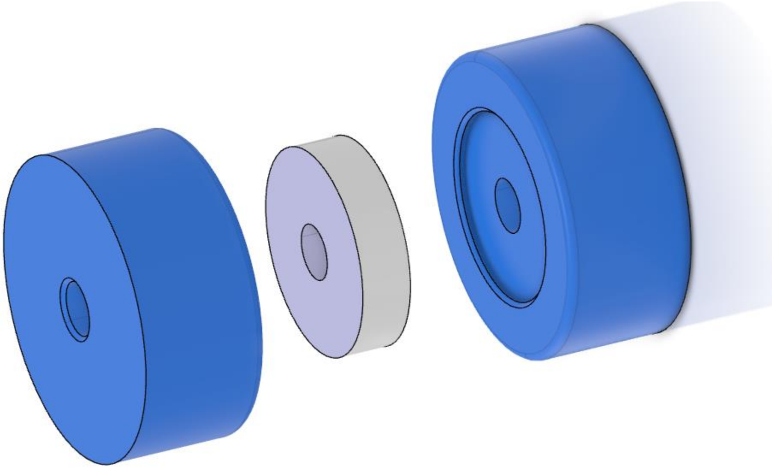

Figure 3.5 Representation of a winding mandrel (white) and limiting mandrels (blue)

The suitable raw materials for the winding and limiting mandrel disks are generally Polytetrafluoroethylene (PTFE / Teflon) or Polyoxymethylene (POM / Delrin) due to the thermal expansion difference. When the wound coil and winding mandrel assembly subjected to a cold environment, the disks shrink more compared to the coil part and the removal process is simplified. Also, the geometric properties of both mandrels are vital such as assembly interfaces, smooth surfaces and sharp edges to prevent fiber sliding and fiber breakage (Figure 3.6).

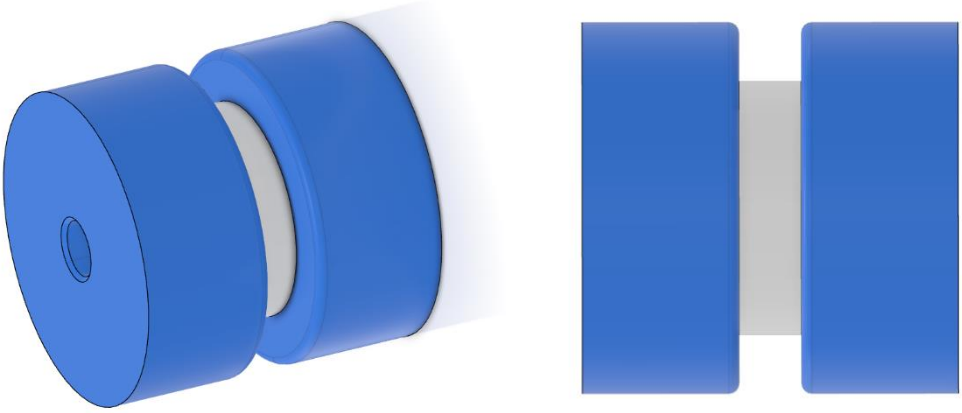

Figure 3.6 Mandrel assembly to start winding process

The blue limiting mandrels should have smooth edges to protect the fiber from edge cuts. On the other hand, the white winding mandrel should have sharp edges on both ends to prevent fiber defects. Likewise, the fiber climbing, fiber gapping, fiber overlapping, winding asymmetry, tensional changes may occur in the winding stage. In order to prevent these errors, each fiber turn is guided from a human operator with the help of a soft stick to arrange the fibers from first line to the end. In order to match the winding mandrel height with an integer number of turns, a small space should be left between the fibers. Furthermore, if there is not enough space between the fibers on the first layer, it can cause some winding defects when laying the next row of the fiber. The right amount of space should be left between the fibers depending on the diameter of the fiber. Generally, the optimal space is between 2% and 5% of the fiber diameter (Figure 3.7).

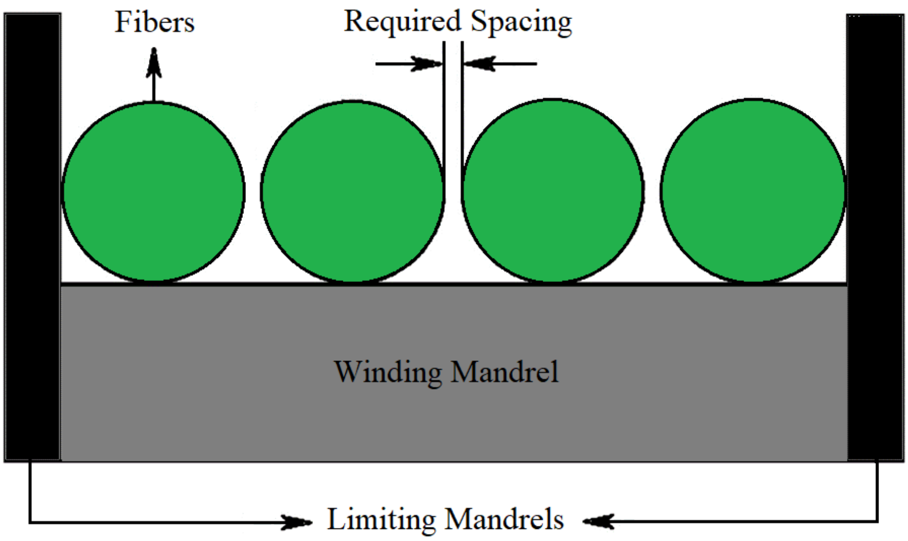

Figure 3.7 Cross sectional representation of a fiber winding process

Before the winding starts, the required total length of the fiber must be calculated based on the determined geometric dimensions in order to reduce the Shupe Effect which is mentioned before in Section 2.2. The total layer count is multiple of four in a quadrupolar winding and should start from the midpoint location of the total fiber length with one half length of the fiber ready to wound on one reel when the other half is ready on the other reel (Figure 3.8).

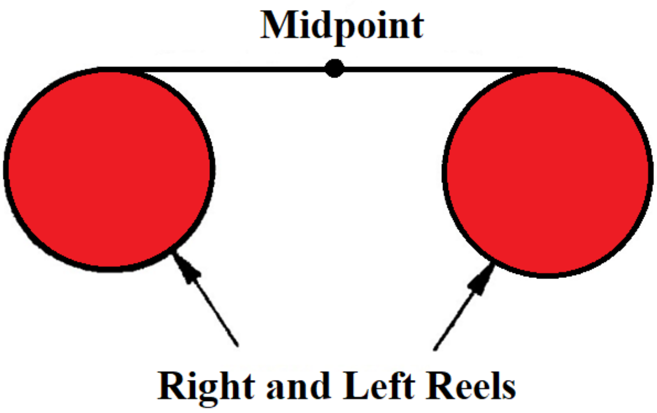

Figure 3.8 Starting point of a quadrupolar winding process

Throughout the winding process, one reel feed the fiber while the other reel is waiting on hold position as shown in Figure 3.9 to arrange the light propagation directions. The changes experienced by one of the light beams propagating through a direction in the core of the fiber are identical to the other light beam propagating on the opposite direction. If a temperature change is occurred at a specific point or a region, the light beams experience the perturbation at the same time and the same distance from the midpoint of the fiber.

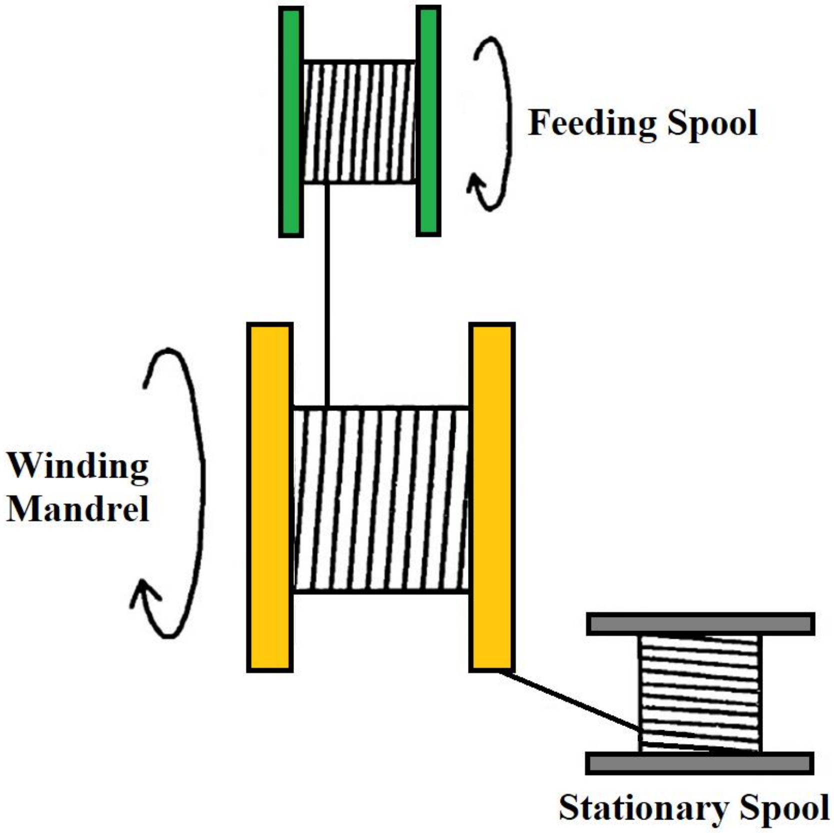

Figure 3.9 Clockwise winding stage of the quadrupolar winding method

The feeding reel (spool) should stop feeding when the other spool starts feeding the fiber to wind the opposite direction layers as shown in Figure 3.10. When the wound fibers recombined, the two propagating light beams should only reflect the phase shift due to rotation of the fiber optic coil.

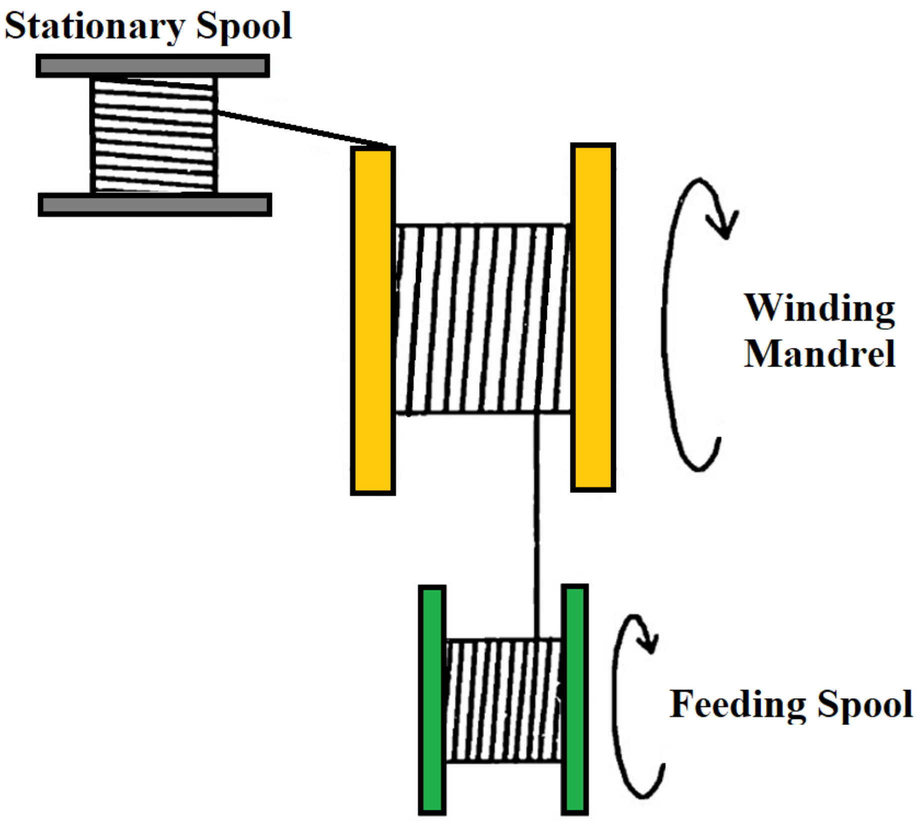

Figure 3.10 Counter clockwise winding stage of the quadrupolar winding method

During the winding process, it is necessary to keep the tensile force constant on the fiber. Increased fiber tension can help defect free winding. On the other hand, the performance of the FOG will degrade under high tension levels on the fiber because of probable non-symmetric mechanical stresses [42]. Typical force values that should be applied to the fiber are between 0.05 Newtons and 0.1 Newtons for a qualified and high-performance FOG coil [43, 63].

In order to make a free stand coil, it is necessary to apply the optical epoxy adhesive between the fibers during the winding process. This procedure is generally human guided and operated under using a soft brush to apply the adhesive. Also, a stick is used to arrange the fiber packaging and prevent the vacancies of adhesive. There are a few high-tech fiber winding devices that have image processing and autonomous winding capabilities which need no human source.

The final stage of the winding process should look like Figure 3.11 that two fiber ends facing the opposite directions on the outside of the coil.

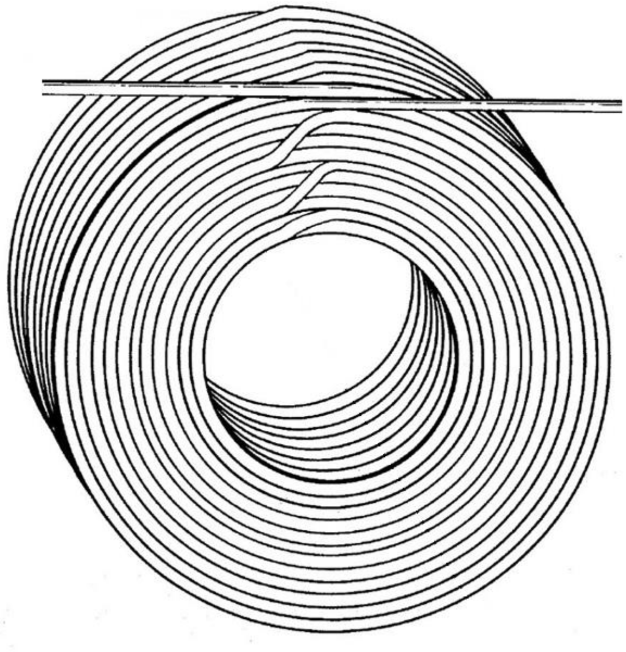

Figure 3.11 Final stage representation of quadrupole wound FOG coil

After the winding stage is finished, the pre-curing process of the adhesive is applied to the mandrel and coil assembly. The pre-curing process is done at approximately 35 °C for at least 24 hours. In this stage, the adhesive mixture initiates to gel and construct some arrangement with the fibers. After that, the limiting mandrels removed from both sides of the coil assembly, and then the coil and the winding mandrel assembly is left to a cold environment. The winding mandrel is then disassembled from the coil with the help of the thermal expansion coefficient difference between the winding mandrel and the coil. The removed coil is called as a free stand coil.

The free stand coil is subjected to a ripening process for final curing approximately six hours as shown in Figure 3.12. Then, the coil is left to room temperature to cool down and the curing process is completed.

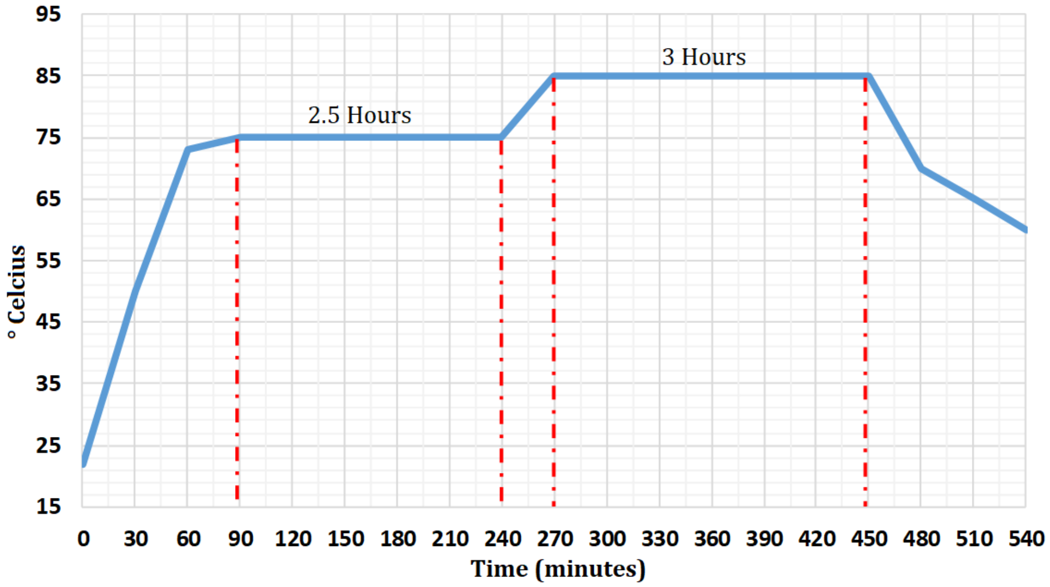

Figure 3.12 Ripening process for a free stand coil production

3.1.3 The Produced Coil Types in This Study

There are two types of fiber optic coils in this study named as Type-1 and Type-2 respectively for their order of testing and production.

3.1.3.1 Coil Type-1

Type-1 coils are produced with the quadrupole winding method. The fibers used in the coil Type-1 is defined in Table 3.1.

The geometric parameters of Coil Type-1 can be seen in Table 3.2. There are five identical coils with the same dimensions for the tests, and the dimensions are the average values of the test batch (Figure 3.13).

Table 3.2 Dimensions for Type-1 quadrupole wound coils (Figure 3.13).

Inner Radius	Outer Radius	Thickness
32.3 mm	38.35 mm	11.9 mm

Figure 3.13 Type-1 fiber-optic coil

3.1.3.2 Coil Type-2

Type-2 coils are produced with the same quadrupole winding method. The fibers used in the Type-2 coil batch are the same with Type-1 coil batch. The geometric parameters of Type-2 coils can be seen in Table 3.3. There are five identical coils with the same dimensions for the tests, and the dimensions are the average values of the test batch.

Table 3.3 Dimensions for Type-2 quadrupole wound coils (Figure 3.14).

Inner Radius	**Outer Radius**	**Thickness**
32.3 mm	36.05 mm	11.9 mm

Figure 3.14 Type-2 fiber-optic coil

Fiber-optic coils are produced with the automated winding machine on a mandrel with two housing Delrin disks at both ends through the manual guidance of the technician to the fibers. Throughout the winding process, the adhesive between the fibers is applied with a brush, so the coils have small structural differences, causing slight dynamic behavioral differences for each coil.

3.2 Homogenization Method

The classical representation of linear anisotropic elasticity states that 21 independent constants of the 6 × 6 stiffness matrix, as shown in Equation (3.3), need to be reduced from the most general anisotropic material to the real case:

$$\begin{Bmatrix} \sigma_1 \\ \sigma_2 \\ \sigma_3 \\ \sigma_4 \\ \sigma_5 \\ \sigma_6 \end{Bmatrix} = \begin{bmatrix} C_{11} & C_{12} & C_{13} & C_{14} & C_{15} & C_{16} \\ C_{21} & C_{22} & C_{23} & C_{24} & C_{25} & C_{26} \\ C_{31} & C_{32} & C_{33} & C_{34} & C_{35} & C_{36} \\ C_{41} & C_{42} & C_{43} & C_{44} & C_{45} & C_{46} \\ C_{51} & C_{52} & C_{53} & C_{54} & C_{55} & C_{56} \\ C_{61} & C_{62} & C_{63} & C_{64} & C_{65} & C_{66} \end{bmatrix} \begin{Bmatrix} \epsilon_1 \\ \epsilon_2 \\ \epsilon_3 \\ \gamma_4 \\ \gamma_5 \\ \gamma_6 \end{Bmatrix} \tag{3.3}$$

The most general Hooke's Law matrix equation $\sigma = C * \mathcal{E}$ will be reduced to a particular class of anisotropy, i.e., orthotropy by using the invariance equations. The reduction of this matrix depends on the mutually orthogonal planes and the symmetry group of the condition. The equations are simplified in the matrix-vector notation. The solution requires Voigt tensor notation together with the invariance conditions.

In general, composite structures reinforced with parallel fibers display orthotropic material properties at the lamina level (mesoscale). In special cases, such as the hexagonal array, the properties become transversely isotropic. This concept can be specified by stating that a material possesses an axis of symmetry of order n when the elastic moduli remain unchanged for rotations of 2π/n radians about the axis. This situation is shown schematically in Fig. 3.15. The hexagonal array case has such a symmetry about the axis perpendicular to the page for n = 6 (60° increments).

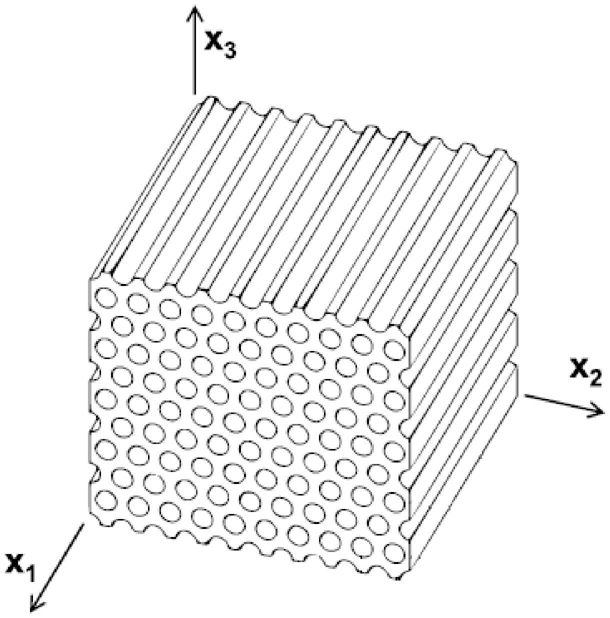

Figure 3.15 Hexagonal array case [51].

In our case, there are spaces between the fibers approximately 2% as explained in Section 3.1.2. Thus, fibers are not arranged with an exact hexagonal array, so the structure shows an orthotropic material behavior. The angle is shown as 61.42° in Figure 3.19 on the selected RVE cell. In this kind of orthotropic linear elasticity case, the elasticity tensor has nine independent coefficients (Equation (3.4)).

$$\begin{bmatrix} C_{11} & C_{12} & C_{13} & 0 & 0 & 0 \\ C_{21} & C_{22} & C_{23} & 0 & 0 & 0 \\ C_{31} & C_{32} & C_{33} & 0 & 0 & 0 \\ 0 & 0 & 0 & C_{44} & 0 & 0 \\ 0 & 0 & 0 & 0 & C_{55} & 0 \\ 0 & 0 & 0 & 0 & 0 & C_{66} \end{bmatrix} \tag{3.4}$$

It is known that the FOG coil is more flexible in the axial and radial directions where the adhesive matrix which stick the fibers together is more resistant in the hoop direction. The material properties of the FOG coil have three symmetry planes, as shown in Figure 3.16. Therefore, the FOG coil structure exhibits orthotropic properties.

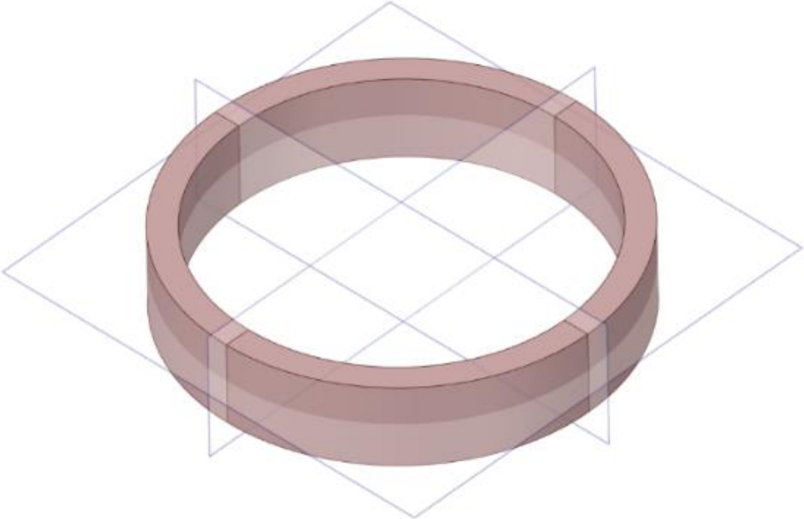

Figure 3.16 Symmetry planes of the fiber optic coil

In this study, an FE model is established using ABAQUS CAE software. The coil is taken as a composite structure. The model uses a homogenization method which is based on modeling the microstructure, and applies the technique to obtain the properties of the composite with the micromechanics method. In the FE model, a representative volume element (RVE) is created as a microstructure, and the global parameters of the composite coil structure are found by this local RVE analysis.

The fiber arrengement in the coil is modeled with two main components. The glass parts of the fiber which are core and cladding behave very similar to each other. The coating part is dual layer acrylate which is a non-glass part and the mechanical contribution to the structure is much less compared to the core and cladding parts. Therefore, the fiber is modeled with glass parts as a united structure with 80 micrometers of diameter while the coating is modeled as the surroundings of glasses with 155 micrometers of diameter as shown in Figure 3.17. The volume percentage of the SAPs are changing depending on the commercial products of different manufacturers. Generally, they are placed both sides of the core continuing along the fiber axis and have approximately the same total volume percentage of the core. In this product, its contribution can be considered as proportional to the 6.5/155 microns and may be considered around 4%. The contribution of the SAPs is neglected due to the fiber rotations during the winding process. The SAPs of Bow-Tie configuration cannot be perfectly aligned with each other along the entire length of the fiber. In this study, their impact is neglected.

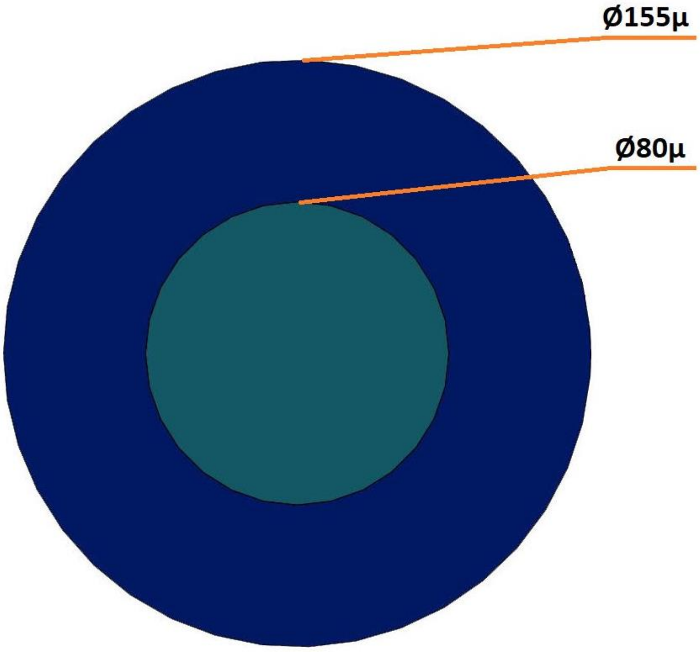

Figure 3.17 The cross section of fiber in the modal analysis

Another assumption made in this study is the effect of the jog zone of the produced coils. Due to the nature of the quadrupole winding method, there occurs a zone between the layers that the fibers are changing their layer from the inner layers to the outer layers as shown in the figure 3.11. This switching zone kept in a small angle in the production stage and exist only the very ends of the coil structure. Hence, the fiber arrangement is assumed to be homogenous between layers, so the jog zone of the quadrupolar winding is neglected in modeling. The FE model is established as identical disks from the inner layer through the outer layer.

In the light of these assumptions, the selected RVE can be seen from the global coil structure of the FE analysis in Figure 3.18.

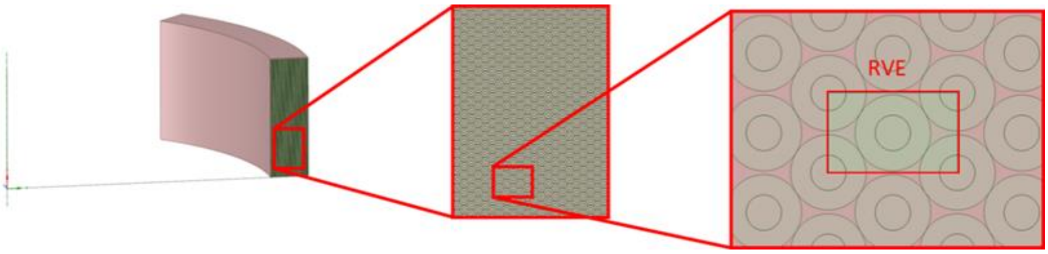

Figure 3.18 Selected representative volume element (RVE) cell from the global coil body.

The RVE selected in this study is shown in Figure 3.19. The red color represents the glass sections, the beige color illustrates the coating of the fibers, and the green color shows the adhesive. The dimensions for the RVE are 266, 158, and 200 µm as the width (Y), height (Z), and depth (X), respectively, for the fiber introduced in Table 3.1. The homogenized RVE results are used in coils introduced in Table 3.2 and Table 3.3.

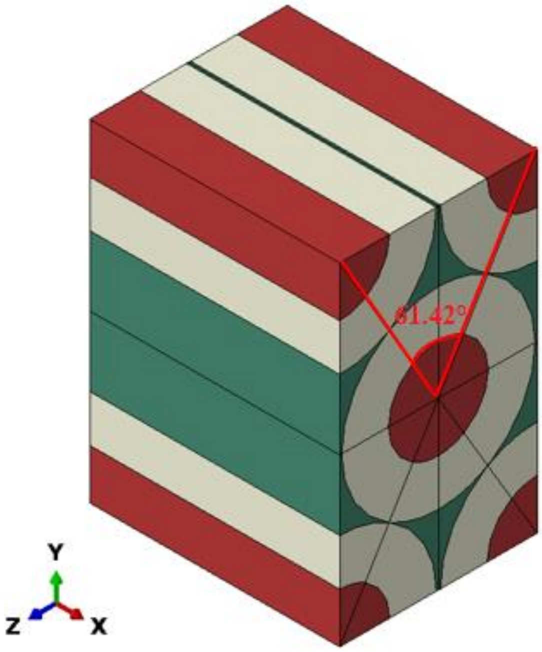

Figure 3.19 Representative volume element (RVE) selected for the actual coil case

The generalized Hooke's Law for the structure shown in Figure 3.19 is given in Equation (3.5) as:

$$\begin{Bmatrix} \bar{\sigma}_1 \\ \bar{\sigma}_2 \\ \bar{\sigma}_3 \\ \bar{\sigma}_4 \\ \bar{\sigma}_5 \\ \bar{\sigma}_6 \end{Bmatrix} = \begin{bmatrix} C_{11} & C_{12} & C_{13} & 0 & 0 & 0 \\ C_{21} & C_{22} & C_{23} & 0 & 0 & 0 \\ C_{31} & C_{32} & C_{33} & 0 & 0 & 0 \\ 0 & 0 & 0 & C_{44} & 0 & 0 \\ 0 & 0 & 0 & 0 & C_{55} & 0 \\ 0 & 0 & 0 & 0 & 0 & C_{66} \end{bmatrix} \begin{Bmatrix} \bar{\epsilon}_1 \\ \bar{\epsilon}_2 \\ \bar{\epsilon}_3 \\ \bar{\gamma}_4 \\ \gamma_5 \\ \bar{\gamma}_6 \end{Bmatrix} \tag{3.5}$$

Furthermore, the RVE should be subjected to displacement boundary conditions in order to obtain components of elasticity matrix C in every direction. The determination of the elements for the C tensor, the components of C_{ij}, can be found one by one throughout the columns. In the following subsections, these calculations are explained.

3.2.1 First Column

In order to calculate the first column of the tensor C, the following procedure is followed.

$$\begin{Bmatrix} \bar{\sigma}_1 \\ \bar{\sigma}_2 \\ \bar{\sigma}_3 \\ \bar{\sigma}_4 \\ \bar{\sigma}_5 \\ \bar{\sigma}_6 \end{Bmatrix} = \begin{bmatrix} C_{11} & C_{12} & C_{13} & 0 & 0 & 0 \\ C_{12} & C_{22} & C_{23} & 0 & 0 & 0 \\ C_{13} & C_{23} & C_{33} & 0 & 0 & 0 \\ 0 & 0 & 0 & C_{44} & 0 & 0 \\ 0 & 0 & 0 & 0 & C_{55} & 0 \\ 0 & 0 & 0 & 0 & 0 & C_{66} \end{bmatrix} \begin{Bmatrix} \bar{\epsilon}_1 \\ 0 \\ 0 \\ 0 \\ 0 \\ 0 \end{Bmatrix} \tag{3.6}$$

By applying this condition to the RVE, the parameters of the first column can be found by

$$\begin{Bmatrix} C_{11} \\ C_{12} \\ C_{13} \end{Bmatrix} = \begin{Bmatrix} \bar{\sigma}_1/\bar{\epsilon}_1 \\ \bar{\sigma}_2/\bar{\epsilon}_1 \\ \bar{\sigma}_3/\bar{\epsilon}_1 \end{Bmatrix} \tag{3.7}$$

The boundary conditions to find the elements of first column of tensor C shows the displacement boundary condition in the X (fiber) direction as

$$\text{X- surface} \qquad U_1 = 0 \tag{3.8}$$

X+ surface $U_1 = 200\mu$

The neighboring RVE cells in Y direction behave the same so there is a symmetry boundary condition in the Y direction as:

$$\begin{array}{ll} \text{Y- surface} & U_2 = UR_1 = UR_3 = 0 \\ \text{Y+ surface} & U_2 = UR_1 = UR_3 = 0 \end{array} \qquad (3.9)$$

The symmetry boundary condition is applied to the Z direction as well.

$$\begin{array}{ll} \text{Z- surface} & U_3 = UR_1 = UR_2 = 0 \\ \text{Z+ surface} & U_3 = UR_1 = UR_2 = 0 \end{array} \qquad (3.10)$$

3.2.2 Second Column

In order to calculate the second column of the tensor C, the following procedure is followed.

$$\begin{Bmatrix} \bar{\sigma}_1 \\ \bar{\sigma}_2 \\ \bar{\sigma}_3 \\ \bar{\sigma}_4 \\ \bar{\sigma}_5 \\ \bar{\sigma}_6 \end{Bmatrix} = \begin{bmatrix} C_{11} & C_{12} & C_{13} & 0 & 0 & 0 \\ C_{12} & C_{22} & C_{23} & 0 & 0 & 0 \\ C_{13} & C_{23} & C_{33} & 0 & 0 & 0 \\ 0 & 0 & 0 & C_{44} & 0 & 0 \\ 0 & 0 & 0 & 0 & C_{55} & 0 \\ 0 & 0 & 0 & 0 & 0 & C_{66} \end{bmatrix} \begin{Bmatrix} 0 \\ \bar{\epsilon}_2 \\ 0 \\ 0 \\ 0 \\ 0 \end{Bmatrix} \qquad (3.11)$$

By applying this condition to the RVE, the parameters of the second column can be found by

$$\begin{Bmatrix} C_{12} \\ C_{22} \\ C_{23} \end{Bmatrix} = \begin{Bmatrix} \bar{\sigma}_1/\bar{\epsilon}_2 \\ \bar{\sigma}_2/\bar{\epsilon}_2 \\ \bar{\sigma}_3/\bar{\epsilon}_2 \end{Bmatrix} \qquad (3.12)$$

The neighboring RVE cells in X direction behave the same so there is a symmetry boundary condition in the X direction as

$$\begin{array}{ll} \text{X- surface} & U_1 = UR_2 = UR_3 = 0 \\ \text{X+ surface} & U_1 = UR_2 = UR_3 = 0 \end{array} \qquad (3.13)$$

The boundary conditions to find the elements of first column of tensor C shows the displacement boundary condition in the X (fiber) direction as

$$\begin{array}{ll} \text{Y- surface} & U_2 = UR_1 = UR_3 = 0 \\ \text{Y+ surface} & U_2 = 266\mu \end{array} \tag{3.14}$$

The symmetry boundary condition is applied to the Z direction as well

$$\begin{array}{ll} \text{Z- surface} & U_3 = UR_1 = UR_2 = 0 \\ \text{Z+ surface} & U_3 = UR_1 = UR_2 = 0 \end{array} \tag{3.15}$$

3.2.3 Third Column

In order to calculate the third column of the tensor C, the following procedure is followed.

$$\begin{Bmatrix} \bar{\sigma}_1 \\ \bar{\sigma}_2 \\ \bar{\sigma}_3 \\ \bar{\sigma}_4 \\ \bar{\sigma}_5 \\ \bar{\sigma}_6 \end{Bmatrix} = \begin{bmatrix} C_{11} & C_{12} & C_{13} & 0 & 0 & 0 \\ C_{12} & C_{22} & C_{23} & 0 & 0 & 0 \\ C_{13} & C_{23} & C_{33} & 0 & 0 & 0 \\ 0 & 0 & 0 & C_{44} & 0 & 0 \\ 0 & 0 & 0 & 0 & C_{55} & 0 \\ 0 & 0 & 0 & 0 & 0 & C_{66} \end{bmatrix} \begin{Bmatrix} 0 \\ 0 \\ \bar{\epsilon}_3 \\ 0 \\ 0 \\ 0 \end{Bmatrix} \tag{3.16}$$

By applying this condition to the RVE, the parameters of the third column can be found by

$$\begin{Bmatrix} C_{13} \\ C_{23} \\ C_{33} \end{Bmatrix} = \begin{Bmatrix} \bar{\sigma}_1/\bar{\epsilon}_3 \\ \bar{\sigma}_2/\bar{\epsilon}_3 \\ \bar{\sigma}_3/\bar{\epsilon}_3 \end{Bmatrix} \tag{3.17}$$

The neighboring RVE cells in X direction behave the same so there is a symmetry boundary condition in the X direction as

$$\begin{array}{ll} \text{X- surface} & U_1 = UR_2 = UR_3 = 0 \\ \text{X+ surface} & U_1 = UR_2 = UR_3 = 0 \end{array} \tag{3.18}$$

The symmetry boundary condition is applied to the Y direction as

$$\begin{array}{ll} \text{Y- surface} & U_2 = UR_1 = UR_3 = 0 \\ \text{Y+ surface} & U_2 = UR_1 = UR_3 = 0 \end{array} \tag{3.19}$$

To find the elements of third column of tensor C, the displacement boundary condition in the Z direction is applied as

$$\begin{array}{ll} \text{Z- surface} & U_3 = UR_1 = UR_2 = 0 \\ \text{Z+ surface} & U_3 = 158\mu \end{array} \tag{3.20}$$

In the first three columns, a unity displacement boundary condition is applied in positive X, Y, and Z directions, respectively. The rest of the surfaces are subjected to symmetry boundary conditions.

3.2.4 Fourth Column

In the fourth column, only the term C_{44} is different from zero and can be calculated by the following procedure.

$$\begin{Bmatrix} \bar{\sigma}_1 \\ \bar{\sigma}_2 \\ \bar{\sigma}_3 \\ \bar{\sigma}_4 \\ \bar{\sigma}_5 \\ \bar{\sigma}_6 \end{Bmatrix} = \begin{bmatrix} C_{11} & C_{12} & C_{13} & 0 & 0 & 0 \\ C_{12} & C_{22} & C_{23} & 0 & 0 & 0 \\ C_{13} & C_{23} & C_{33} & 0 & 0 & 0 \\ 0 & 0 & 0 & C_{44} & 0 & 0 \\ 0 & 0 & 0 & 0 & C_{55} & 0 \\ 0 & 0 & 0 & 0 & 0 & C_{66} \end{bmatrix} \begin{Bmatrix} 0 \\ 0 \\ 0 \\ \bar{\gamma}_4 \\ 0 \\ 0 \end{Bmatrix} \tag{3.21}$$

By applying this condition to the RVE, the parameters of the fourth column can be found by

$$\{C_{44}\} = \{\bar{\sigma}_4/\bar{\gamma}_4\} \tag{3.22}$$

The surfaces of neighboring RVE cells in X direction lean the same and all the dofs of the nodes on X- surface are coupled to the nodes on X+ surface so this periodic boundary condition in the fiber direction can be defined as

$$\begin{array}{ll} \text{X- surface} & \\ & \mathrm{U}_{i_{x-}} = \mathrm{U}_{i_{x+}} \\ \text{X+ surface} & \end{array} \tag{3.23}$$

To find the elements of fourth column of tensor C, the displacement boundary condition in the Y direction to create the shear behavior is applied as

$$\begin{array}{ll} \text{Y- surface} & U_1 = U_2 = 0 \\ \text{Y+ surface} & U_1 = 266\mu,\ U_2 = 0 \end{array} \tag{3.24}$$

The symmetry boundary condition is applied to the Z direction as

$$\begin{array}{ll} \text{Z- surface} & U_3 = UR_1 = UR_2 = 0 \end{array} \tag{3.25}$$

Z+ surface $U_3 = UR_1 = UR_2 = 0$

3.2.5 Fifth Column

In the fifth column, only the term C_{55} is different from zero and can be calculated by the following procedure.

$$\begin{Bmatrix} \bar{\sigma}_1 \\ \bar{\sigma}_2 \\ \bar{\sigma}_3 \\ \bar{\sigma}_4 \\ \bar{\sigma}_5 \\ \bar{\sigma}_6 \end{Bmatrix} = \begin{bmatrix} C_{11} & C_{12} & C_{13} & 0 & 0 & 0 \\ C_{12} & C_{22} & C_{23} & 0 & 0 & 0 \\ C_{13} & C_{23} & C_{33} & 0 & 0 & 0 \\ 0 & 0 & 0 & C_{44} & 0 & 0 \\ 0 & 0 & 0 & 0 & C_{55} & 0 \\ 0 & 0 & 0 & 0 & 0 & C_{66} \end{bmatrix} \begin{Bmatrix} 0 \\ 0 \\ 0 \\ 0 \\ \bar{\gamma}_5 \\ 0 \end{Bmatrix} \tag{3.26}$$

By applying this condition to the RVE, the parameters of the fifth column can be found by

$$\{C_{55}\} = \{\bar{\sigma}_5/\bar{\gamma}_5\} \tag{3.27}$$

The symmetry boundary condition is applied to the X direction as

X- surface $U_1 = UR_2 = UR_3 = 0$

X+ surface $U_1 = UR_2 = UR_3 = 0$ (3.28)

The surfaces of neighboring RVE cells in Y direction lean the same and all the dofs of the nodes on Y- surface are coupled to the nodes on Y+ surface so this periodic boundary condition in the fiber direction can be defined as

Y- surface

Y+ surface $\mathrm{U}_{i_{y-}} = \mathrm{U}_{i_{y+}}$ (3.29)

To find the elements of fifth column of tensor C, the displacement boundary condition in the Z direction to create the shear behavior is applied as

Z- surface $U_2 = U_3 = 0$

Z+ surface $U_2 = 158\mu, U_3 = 0$ (3.30)

3.2.6 Sixth Column

In the sixth column, only the term C_{66} is different from zero and can be calculated by the following procedure.

$$\begin{Bmatrix} \bar{\sigma}_1 \\ \bar{\sigma}_2 \\ \bar{\sigma}_3 \\ \bar{\sigma}_4 \\ \bar{\sigma}_5 \\ \bar{\sigma}_6 \end{Bmatrix} = \begin{bmatrix} C_{11} & C_{12} & C_{13} & 0 & 0 & 0 \\ C_{12} & C_{22} & C_{23} & 0 & 0 & 0 \\ C_{13} & C_{23} & C_{33} & 0 & 0 & 0 \\ 0 & 0 & 0 & C_{44} & 0 & 0 \\ 0 & 0 & 0 & 0 & C_{55} & 0 \\ 0 & 0 & 0 & 0 & 0 & C_{66} \end{bmatrix} \begin{Bmatrix} 0 \\ 0 \\ 0 \\ 0 \\ 0 \\ \bar{\gamma}_6 \end{Bmatrix} \tag{3.31}$$

By applying this condition to the RVE, the parameters of the sixth column can be found by

$$\{C_{66}\} = \{\bar{\sigma}_6/\bar{\gamma}_6\} \tag{3.32}$$

The surfaces of neighboring RVE cells in X direction lean the same and all the dofs of the nodes on X- surface are coupled to the nodes on X+ surface so this periodic boundary condition in the fiber direction can be defined as

X- surface

X+ surface

$$\mathrm{U}_{i_{x-}} = \mathrm{U}_{i_{x+}} \tag{3.33}$$

The symmetry boundary condition is applied to the Y direction as

Y- surface $\quad U_2 = UR_1 = UR_3 = 0$

Y+ surface $\quad U_2 = UR_1 = UR_3 = 0$ (3.34)

To find the elements of sixth column of tensor C, the displacement boundary condition in the Z direction to create the shear behavior is applied as

Z- surface $\quad U_1 = U_3 = 0$

Z+ surface $\quad U_1 = 158\mu, U_3 = 0$ (3.35)

The general boundary condition notation for the symmetry boundary condition in ABAQUS software applies zero for the rotations but the rotations are not included in the calculations because solid elements are used in FE analysis and there is no rotation dof in the solid elements.

From Figure 3.20., the load cases for applied boundary conditions for the calculation of the columns can be seen from (a), (b), (c), (d), (e), and (f) according to Equations (3.6-3.35).

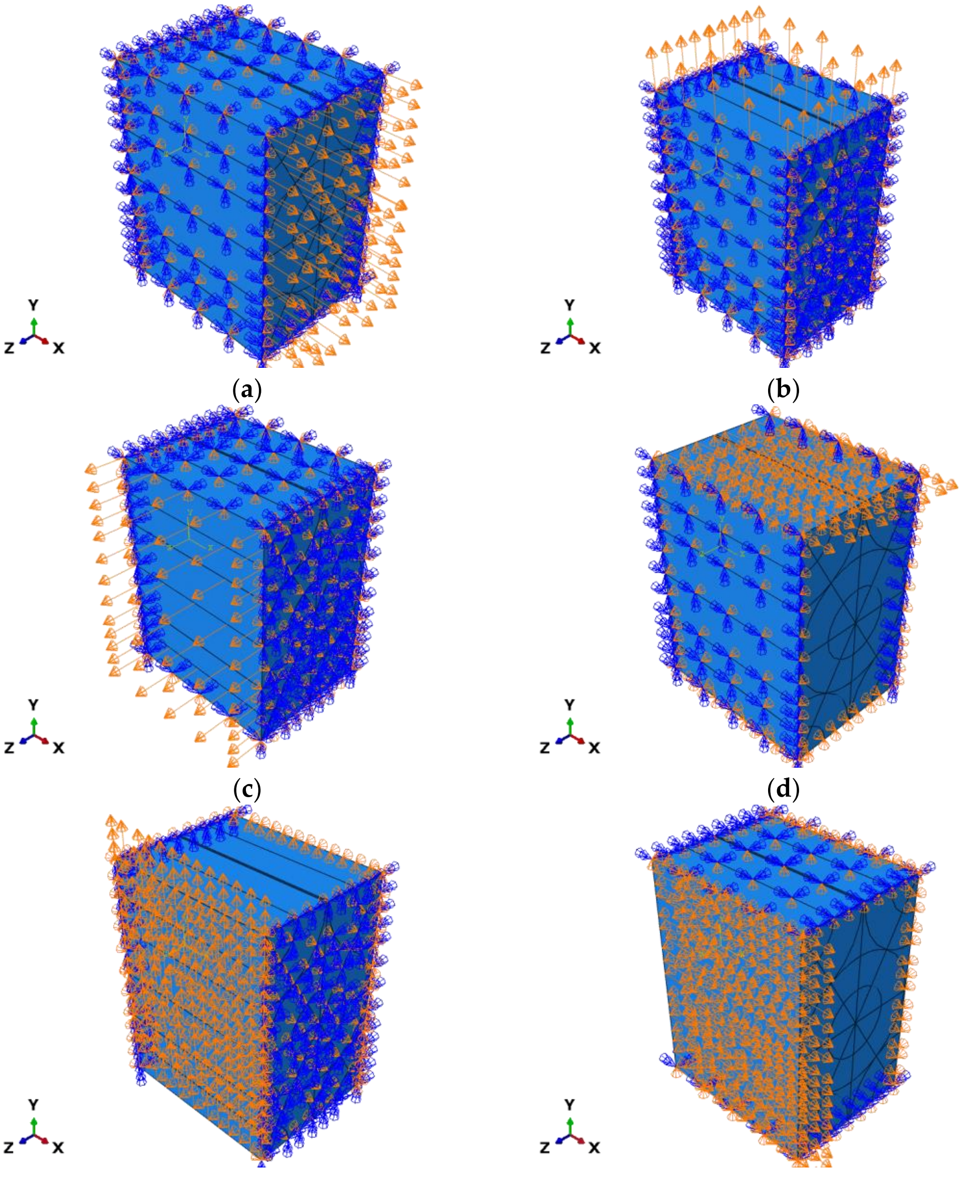

(a) (b)

(c) (d)

(e) (f)

Figure 3.20 The load cases for the solution of the: (a) first column of tensor C; (b) second column of tensor C; (c) third column of tensor C; (d) fourth column of tensor C; (e) fifth column of tensor C; and (f) sixth column of tensor C.

After finding the components of the elasticity matrix, the compliance matrix can be calculated by taking the inverse of the elasticity matrix as

$$[S] = [C]^{-1} \tag{3.36}$$

From the compliance matrix, the overall orthotropic material properties of the selected RVE can be calculated by applying

$$\begin{Bmatrix} \epsilon_{xx} \\ \epsilon_{yy} \\ \epsilon_{zz} \\ \epsilon_{yz} \\ \epsilon_{zx} \\ \epsilon_{xy} \end{Bmatrix} = \begin{bmatrix} 1/E_1 & -\nu_{21}/E_2 & -\nu_{31}/E_3 & 0 & 0 & 0 \\ -\nu_{12}/E_1 & 1/E_2 & -\nu_{32}/E_3 & 0 & 0 & 0 \\ -\nu_{13}/E_1 & -\nu_{23}/E_2 & 1/E_3 & 0 & 0 & 0 \\ 0 & 0 & 0 & 1/2G_{23} & 0 & 0 \\ 0 & 0 & 0 & 0 & 1/2G_{31} & 0 \\ 0 & 0 & 0 & 0 & 0 & 1/2G_{12} \end{bmatrix} \begin{Bmatrix} \sigma_{11} \\ \sigma_{22} \\ \sigma_{33} \\ \sigma_{23} \\ \sigma_{31} \\ \sigma_{12} \end{Bmatrix} \tag{3.37}$$

The resulting global material parameters and the results of the RVE load cases are given in the Section 4.1.

3.3 Modal Test Methodology

The experimental modal testing approach is utilized to obtain the natural frequencies and mode shapes of the composite coil structure for Coil Type-1 and Coil Type-2. The results of these modal tests are discussed in Section 4.3 for both coil configurations.

Modal analysis is an experimental process that the natural characteristics of a structure is described by the frequency, damping and mode shapes. Understanding both the mode shapes and natural frequencies of a structural system helps to design against noise and vibration loadings [61].

In order to visualize the measurement, a freely supported beam in Figure 3.21 is selected as an example. If an input force is applied to the beam in a sinusoidal function, and changed the rate of sinus, it will cause a peak force among the beam and the force will always be the same value. The response of the excitation is measured with an accelerometer at the tip of the beam.

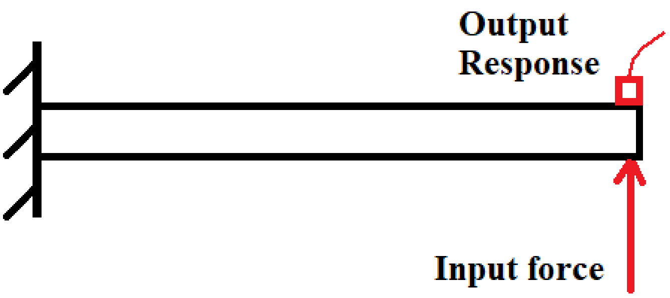

Figure 3.21 Flat plate excitation/response example

The amplitude of the measured response changes as we change the frequency of the input. There will be decreases and increases in time axis (Figure 3.22). This may seem unexpected since the force is constant. However, it is the amplifying response as a result of applied constant force with a rate of oscillation which gets closer to the natural frequency of the system. It reaches its maximum value when the rate of oscillation is exactly at the resonant frequency of the beam.

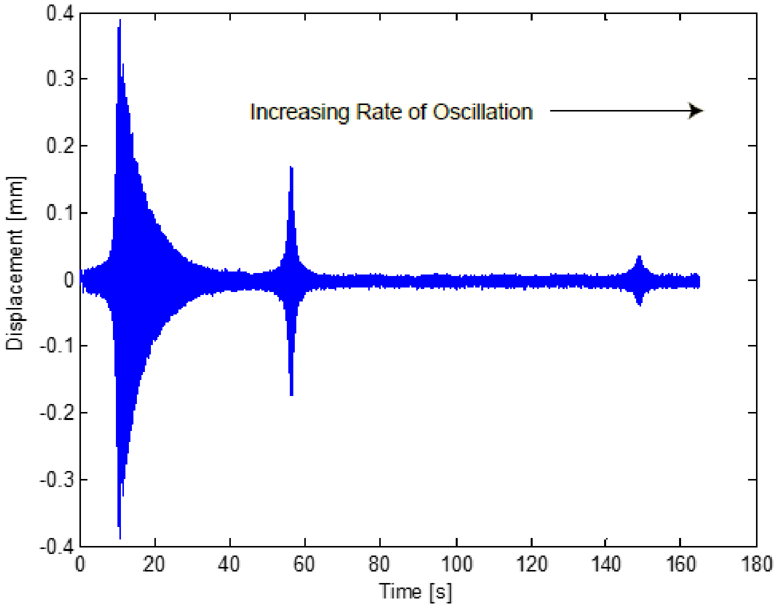

Figure 3.22 Typical time data example of a beam [64]

The time data provides useful information if it is transformed to the frequency domain using Fast Fourier Transform (FFT). The Frequency Response Function

(FRF) then can be calculated. The FRF is the ratio of the output response of a structure to the applied force [61]. Both the applied force and the response of the structure are measured due to the applied force at the same time. This simultaneously measured time data is then transformed from the time domain to the frequency domain by using FFT algorithm (Figure 3.23). This algorithm can be found in any signal processor and their software packages.

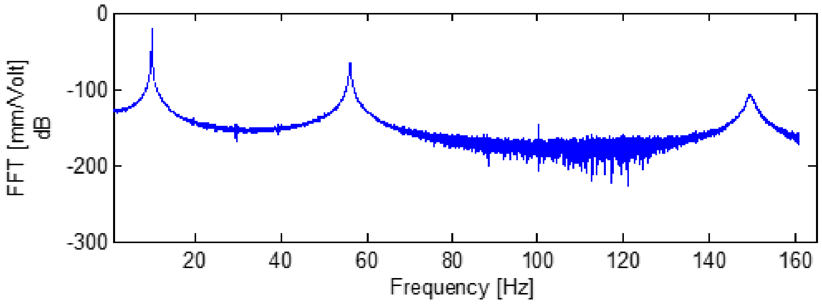

Figure 3.23 FRF graph of the beam [64]

When we plot the graphs on top of each other, it can be seen that the frequency of oscillation when time trace reaches maximum value corresponding to the frequency where the peaks in the FRF reaches their maximum value (Figure 3.24).

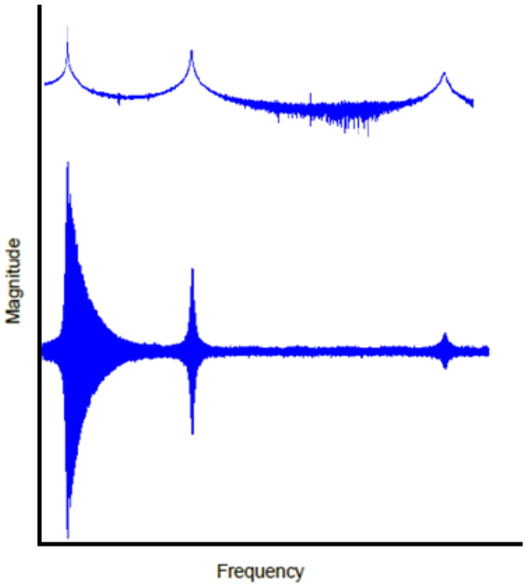

Figure 3.24 Time and frequency graphs together [64]

It is clear that, the FRF function is way easier to evaluate than the time data. Suppose that sufficient number of accelerometers are evenly placed on the plate, there will be a viewable deformation pattern that exists on the plate structure. Each one of the peaks will correspond to a different mode shape (Figure 3.25). As a designer, one should identify these frequencies and should know how they might affect the response of the designed structure when the system is excited by a force or a vibrational loading [59,60,61].

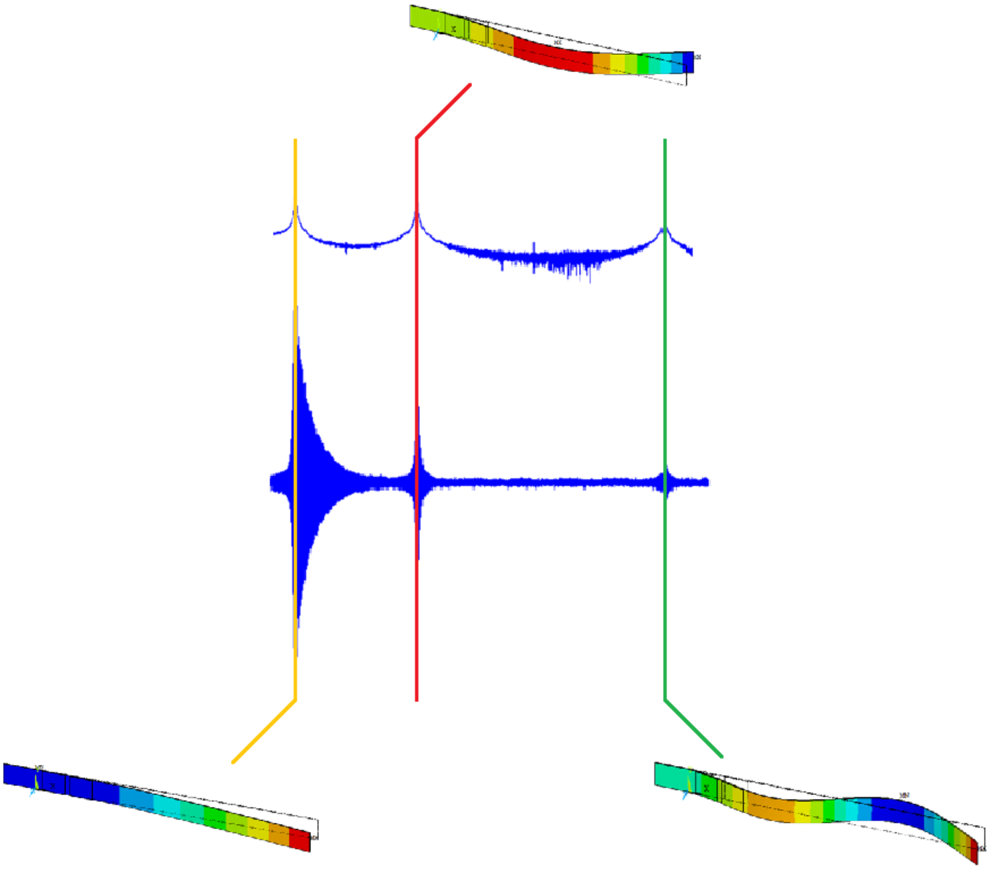

Figure 3.25 Beam responses as mode shapes

The FRF matrix is symmetric due to the fact that the mass, damping and the stiffness matrices that describes the system are symmetric. Therefore, it is possible to obtain all the terms in the FRF matrix by measuring only one row or column of it. During the data collection process, if the point where the input force is given and the point where the measurement is made are the same, the graphic derived from the frequency response of this specific point is called as a drive point FRF. The most important characteristics of a drive point FRF is all resonances are seperated by anti-resonances. In this scenario, the graphic gives a clear understanding and the natural frequencies can be comprehensed easily.

The aim of this experimental study is to collect data on the FOG coil in order to analyze the dynamic behavior of the coil and reveal the mode shapes of the composite coil structure. In impact hammer modal testing, the impact hammer and accelerometer time domain measurements are acquired simultaneously upon impact. The hammer provides an impact to the structure to excite the modes as an input, and a necessary and sufficient number of accelerometers collect the vibration acceleration data from the structure as an output. The frequency response functions in this study are obtained by dividing the Fourier transform of the accelerometer data by the hammer data with respect to frequency. The FRF serves as a transfer function between excitation and response. With the help of a measured set of FRFs, one can obtain the natural frequencies, mode shapes, and damping ratios of a physical structure for a selected set of modes by a procedure called experimental modal analysis (EMA) [59,60]. In order to observe the mode shapes of the structure, a sufficient amount of reference points must be used for data acquisition. From FRF plots, the resonant frequencies of a structure can be spotted and the damping ratios can be deduced. The damping of the structure at the peaks in the FRF graph is proportional to the width of the peaks. The wider the peak, the heavier the damping. Tests are performed using the LMS SCADAS data acquisition system. Before the modal tests, eight locations are marked on the coils with 45-degree angles around the radial direction. Red dots show the hammer-hitting locations and the accelerometer positions (Figure 3.26).

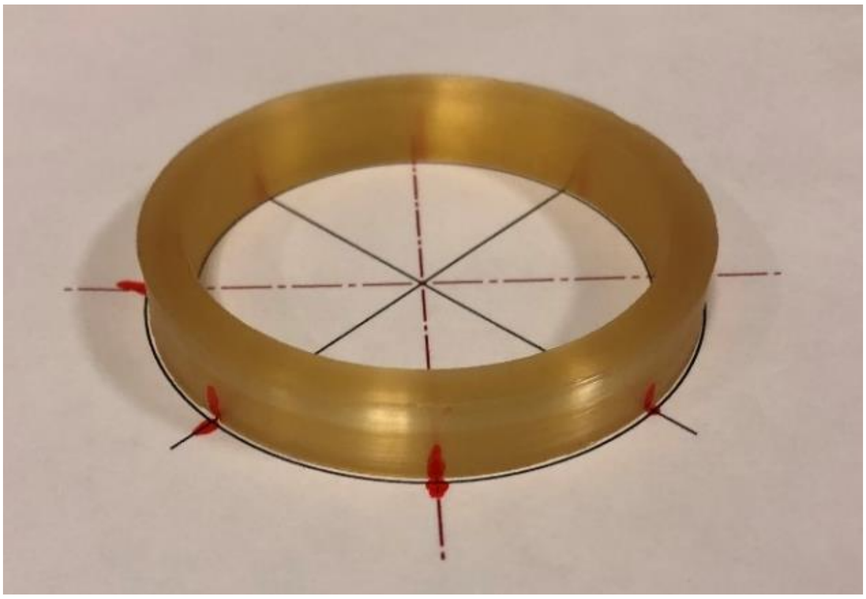

Figure 3.26 Hammer-hitting locations

Tests are carried out in two stages, representing the hitting directions of the hammer to excite the structure in different directions to reveal the modal shapes better. In Figures 3.27 and 3.28, both hitting directions can be seen when the impact hammer of the modal test robot is located in the hoop and the axial direction. In the modal tests, four one-axis accelerometers are placed on two axial and two rear (hoop) sides of the coil. Points are numbered from 1 to 8 on the coil substances by 45-degree intervals along the circumference of the coil. Point number 1 is the hammer hitting location in the tests.

The coil is subjected to free-free boundary condition in the modal tests. The coil is hanged from the both ends with the help of rubber bands to setup the free-free boundary condition.

At the first stage, the impact hammer is placed on the rear (hoop) side of point 1, while the 4 accelerometers are located at points 1 and 5 at the hoop and axial directions (Figure 3.27). The accelerometers are then moved to points 2 and 6, points 3 and 7, and points 4 and 8, respectively. Next, the first stage of the modal test is completed by the fixed hammer location at the hoop side excitation.

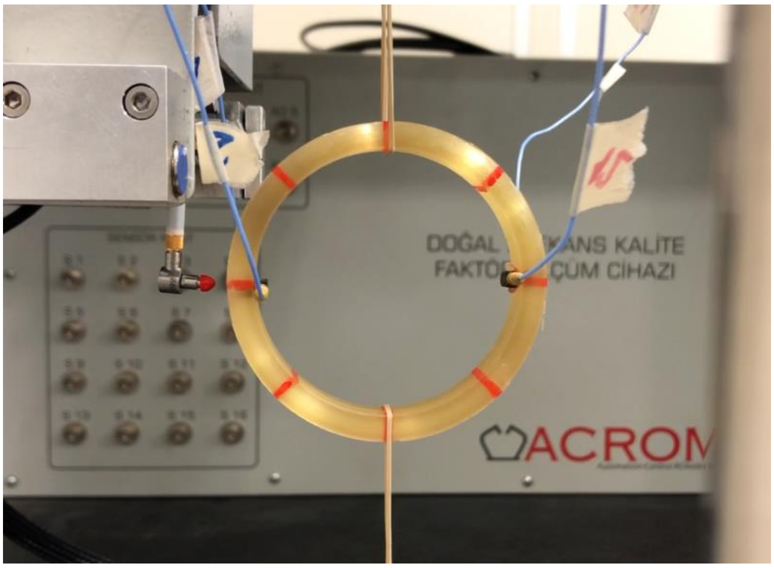

Figure 3.27 The first stage of the impact modal test

At the second stage, the impact hammer excitation is generated from the axial side of the coils (Figure 3.28). The excitation given from the axial side will give a clean separation of out of plane modes in the drive point FRFs of the hitting location. When the hammer is placed at point 1, the accelerometers are placed at points 1 and 5 at the hoop and axial axis directions, and the moving accelerometer procedure follows as mentioned in the first stage.

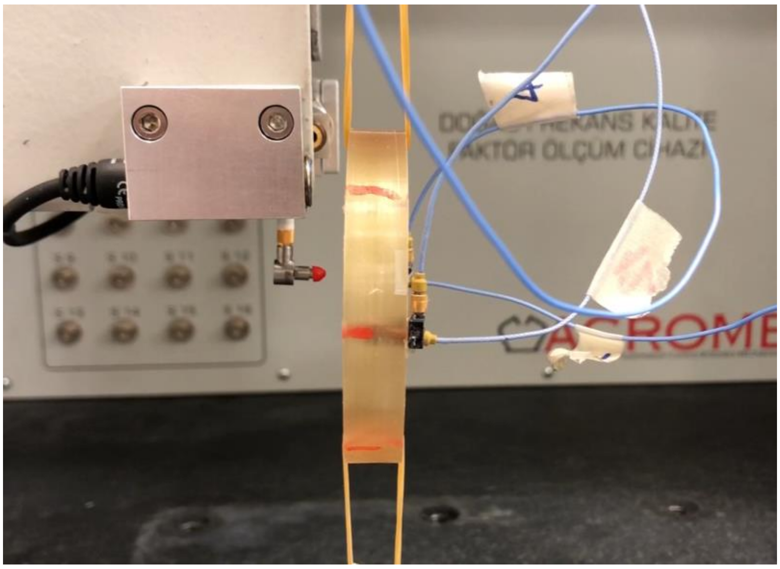

Figure 3.28 The second stage of the impact modal test

The impact hammer triggers the mode shape of the structure in the same direction where it is excited, while the mode shapes of the other direction are not triggered enough, so the excitation must be given in two directions. Merging the data from each excitation test produces the best behavior for the coil samples if they are evaluated in the same basket. The mode shapes of these structures are displayed with this method.

The tests are carried out with ICP-type single-axis mini PCB-Piezotronics accelerometers for all configurations. There are eight accelerometers available that have average actual sensitivities of approximately 5.2 mV/g. The data acquisition system has eight channel inputs, and one channel is reserved for the impact hammer, so there are seven channels left to the accelerometers. Therefore, one impact hammer and four accelerometers are used to carry out the tests. The structures acquisition module of LMS Test Lab software is used to process the acquired data (Figure 3.29).

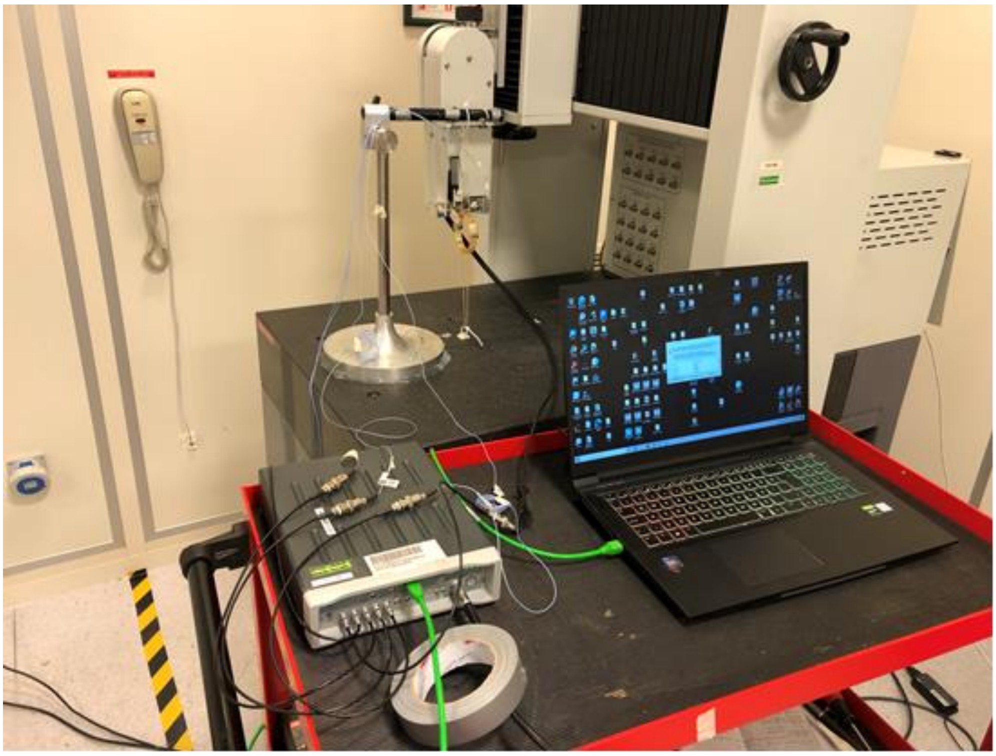

Figure 3.29 Modal test robot and data acquisition test setup.

In order to minimize data collection errors, an automated Modal Test Robot (MTR) is used during the data acquisition process. Intended use of MTR is to keep the excitation given to the structure stable. If the tip of the hammer hits the structure harder or smoother compared to the defined threshold, the data gets mixed up especially in the modal regions. Likewise, the orientation of the hammer tip should be adjusted in order to prevent non-axial loadings in the structure. Besides, the movement direction should be kept constant when hitting the coil. If these are not automated by a robot, incomprehensible data sets can be obtained. In Figure 3.29, the data acquisition test setup and the MTR can be seen with the coil adjusted to free-free boundry condition.

The same two-stage testing process is also carried out for both the Type-1 and Type-2 coil batches. Due to the slight production differences between the coils, differences in the resonance frequencies can be observed. The standard deviation of the modal test results are mentioned in Section 4.3.

CHAPTER 4

ANALYSIS AND TEST RESULTS

In order to obtain the orthotropic elastic properties of the FOG coil, an RVE approach is employed, as mentioned in Section 3.2. The global homogenized material properties calculated through the homogenization procedure and these material properties are fed into the global FE model of the FOG coil for both coil configurations. The natural frequencies and mode shapes of the coils are calculated by means of modal analysis. After the comparison of the FOG coil modal analysis results with the experimental modal test results, the homogenized orthotropic material properties of the FOG coil are verified.

4.1 RVE Analysis Results

In this subsection, the finite element analysis results of the RVE are discussed. The components of tensor C are used to find the homogeneous material properties.

In the computation of the homogenized orthotropic material properties of the RVE, unit strains are applied in each direction by employing the boundary conditions explained in Section 3.2 (Figure 4.1). The calculated stress results in the elements of the RVE are integrated through the volume of the elements and divided by the total volume of the RVE cell. The stiffness matrix of the RVE is obtained with this procedure. By taking the inverse of the stiffness matrix, the compliance matrix is found and equivalent homogenized orthotropic material properties are calculated with Equations (3.6)–(3.37). These results are tabulated in Table 4.1.

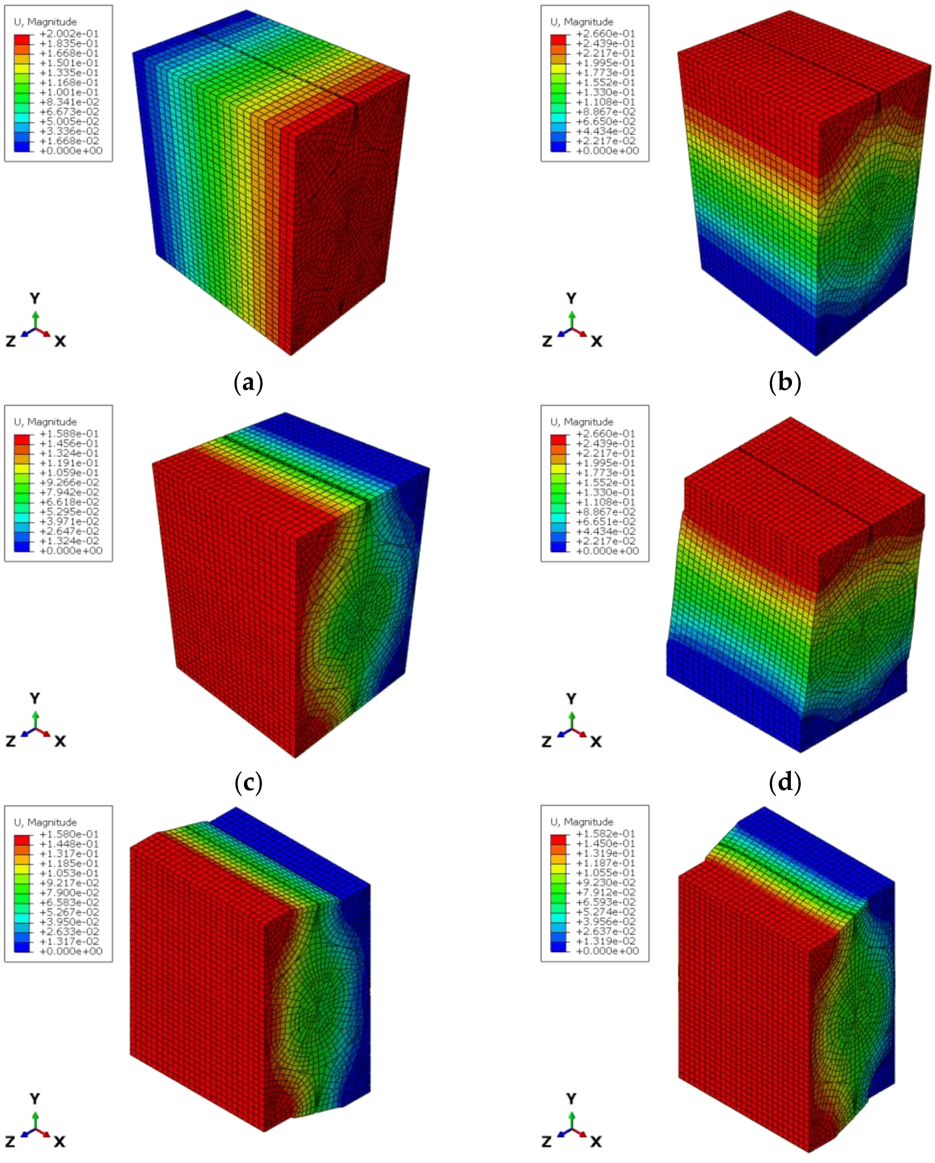

(**a**) (**b**)

(**c**) (**d**)

(e) (f)

Figure 4.1 Displacement results (in mm) for the: (a) first column of tensor C; (b) second column of tensor C; (c) third column of tensor C; (d) fourth column of tensor C; (e) fifth column of tensor C and (f) sixth column of tensor C.

Table 4.1 Global material properties obtained from the RVE model (MPa).

E_1	**E_2**	**E_3**	**ν_{12}**	**ν_{13}**	**ν_{23}**	**G_{12}**	**G_{13}**	**G_{23}**
16893	622	626	0.013	0.013	0.596	134	222	165

The homogenized orthotropic material properties given in Table 4.1 are used in the global coil FE model in cylindrical coordinates. The units of Young's and shear modulus are given in MPa.

A standard linear element type is used in the RVE cell model. In total, 27326 nodes and 24750 linear hexahedral of type C3D8R elements are used in the RVE. The C3D8R element has eight node linear bricks and reduced integration with hourglass control. This element can be used in static deflection analysis [65]. Because of the loading is linear, there is no bending, and the analysis is done in the linear elastic regime, linear elements are sufficient for the cell.

4.2 Modal Analysis Results

In this subsection, the global FE model results for each coil case are discussed. The calculated homogenized orthotropic material properties from the RVE model are used as input parameters for both the coil Type-1 and coil Type-2 global FE models. The global FE models contain the homogenized coil material properties and the geometrical properties for the coil. The FE results of coil Type-1 and coil Type-2 are discussed in Section 4.2.1 and Section 4.2.2 respectively.

4.2.1 Modal Analysis Results for Coil Type-1

The natural frequencies and mode shapes for the coil Type-1 from the global FE model are calculated by applying the global orthotropic material properties obtained from the RVE model as the input material parameter set. The mode shapes obtained from the FE analysis results of the Type-1 coil configuration are given below in Figure 4.2. The mode shapes are the eigenvalues of the modal analysis results and represents the dynamic behavior of the Type-1 coil.

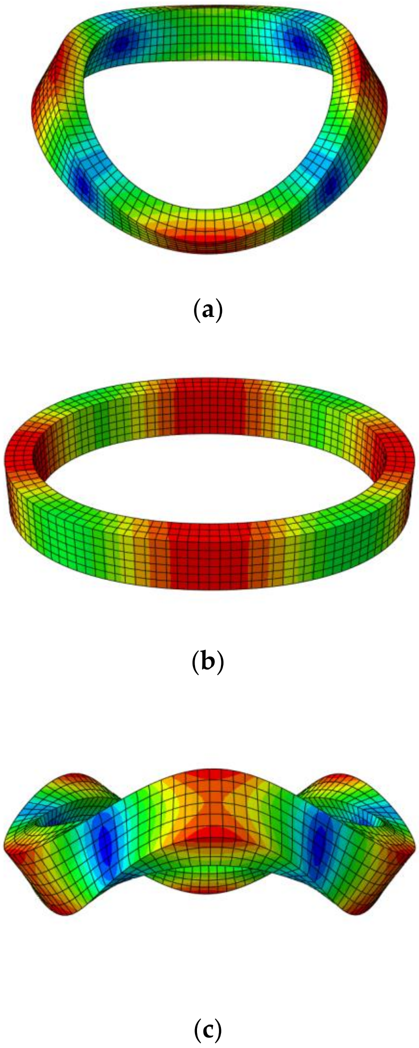

Figure 4.2 Mode shapes for the coil Type-1: (a) first mode shape; (b) second mode shape; (c) third mode shape.

The natural frequency values found from the FE model of the coil Type-1 are tabulated in Table 4.2 as the first, second and third natural frequencies.

Table 4.2 Natural frequency results from modal analysis of coil Type-1

	Mode 1	**Mode 2**	**Mode 3**
Modal Analysis	761.62 Hz	1535.9 Hz	2328.5 Hz

A quadratic element type is used in the global coil FE model where 11312 nodes and 2016 C3D20 elements are used in the Type-1 FE model. The C3D20 element is twenty node quadratic bricks. This is an excellent element for linear elastic calculations [65]. There are 3 elements in the thickness and 6 elements in the width of the coil. This meshing configuration became adequate in bending loadings such that finer meshes such as 4 and 5 elements in the thickness did not change the resonance frequencies. The differences in the mode 1 and mode 2 values are below 0.02 % and the difference in mode 3 value is 0.04 %.

4.2.2 Modal Analysis Results for Coil Type-2

The natural frequencies and mode shapes for the coil Type-2 from the global FE model are calculated by applying the global orthotropic material properties obtained from the RVE model as the input material parameter set. The mode shapes obtained from the FE analysis results of the Type-2 coil configuration are given below in Figure 4.3. The mode shapes are the eigenvalues of the modal analysis results and represents the dynamic behavior of the Type-2 coil.

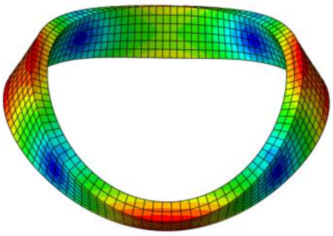

(**a**)

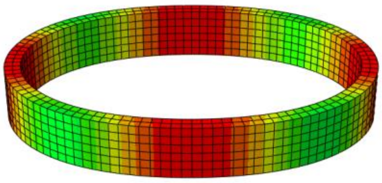

(**b**)

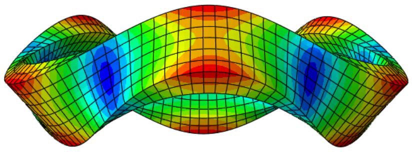

(c)

Figure 4.3 Mode shapes for the coil Type-2: (a) first mode shape; (b) second mode shape; (c) third mode shape.

The natural frequency values of the coil Type-2 simulated in FE model are tabulated in Table 4.3.

Table 4.3 Natural frequency results from modal analysis of coil Type-2

	Mode 1	**Mode 2**	**Mode 3**
Modal Analysis	604.82 Hz	1173.1 Hz	2071.2 Hz

A quadratic element type is used in the global coil FE model where 8066 nodes and 1308 C3D20 elements are used in the Type-2 FE model. There are 2 elements in the thickness and 6 elements in the width of the coil. This meshing configuration became adequate in bending loadings such that finer meshes such as 3 and 4 elements in the thickness did not change the resonance frequencies. The differences in the mode 1 and mode 2 values are below 0.18 % and the difference in mode 3 value is 0.29 %.

4.3 Modal Test Results

In this section, the results of the modal tests for both the Type-1 and the Type-2 coil configurations are discussed respectively. The results are gathered and presented in a table for each subsection. Then, these modal test results are compared with the modal analysis results for the corresponding coil configuration in Section 4.4.

4.3.1 Modal Test Results of Coil Type-1

The mode shapes and resonance frequencies for the Type-1 coil are evaluated. In the testing scheme, the axis definitions for a coil sample are: +X is the outward radial direction; and –X is the direction towards the center of the coil circle. +Z and –Z give the direction out-of-plane when the coil is placed on the table, as shown in Figure 3.26.

Figure 4.4 shows the drive point FRF result graph for a Type-1 coil. The drive point measurement is when the given excitation and collected data are at the same reference point and direction.

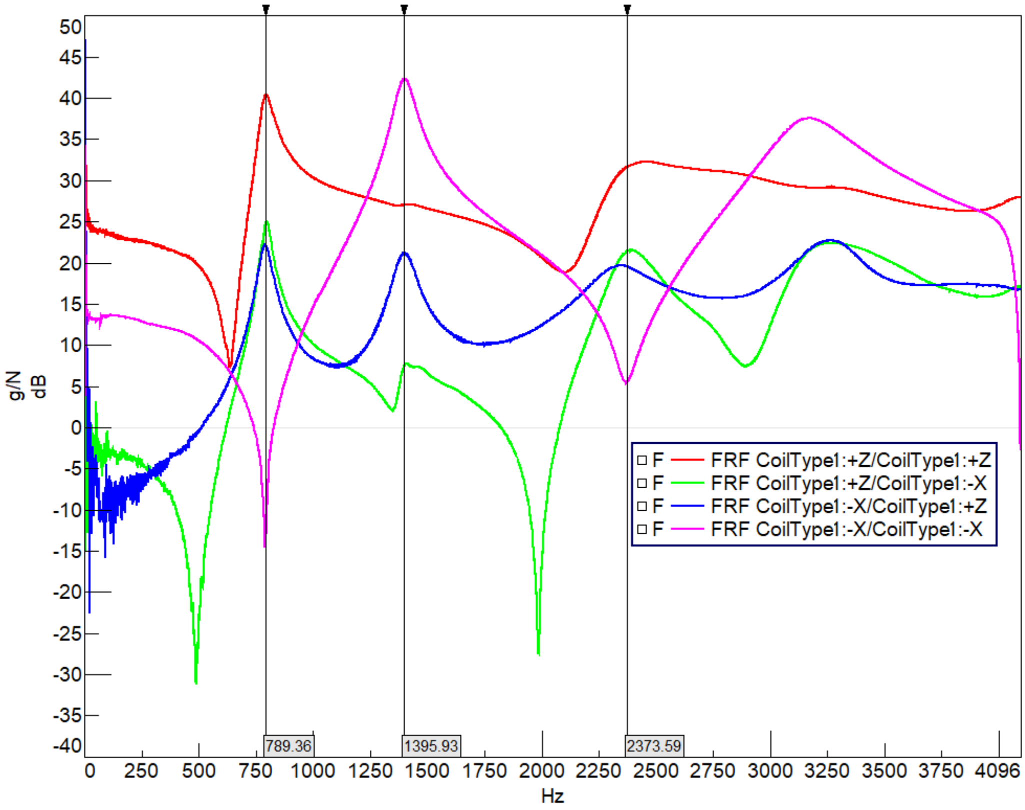

Figure 4.4 Drive point FRF for Coil Type-1.

The OX axis is frequency (Hz) and the OY axis is frequency response (g/N) shown in decibels (dB) in Figure 4.4. The input from the hammer at point 1 and the response output from the accelerometer at point 1 in the ¬–X direction (pink function) gives the modes in the radial direction mode shape frequencies as the peaks. This means the pink function shows an in-plane mode shape and a resonance movement at 1395 Hz, while the 789 Hz and 2373 Hz show an anti-resonance. Therefore, it can be seen from the FRF that there will be a radial movement of the coil structure as the second mode, while the first and third modes are oriented in an out-of-plane (Z) direction. In addition, the red line is the FRF curve for the out-of-plane (Z) excitation and response. The main peak points for the structure occur at the 789 Hz and 2373 Hz values as the first and third modes, so the out-of-plane bending modes are located at these frequencies [66].

The blue lines represent the deformed shape for the natural, while the black dashed lines represent the undeformed shape of the Coil Type-1 in Figures 4.5–4.7.

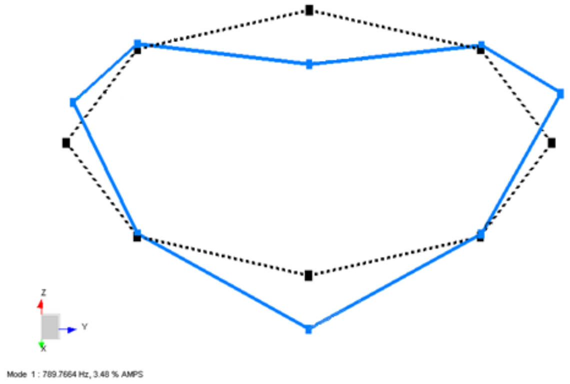

Figure 4.5 First mode shape obtained from LMS Test Lab software for a Type-1 coil sample.

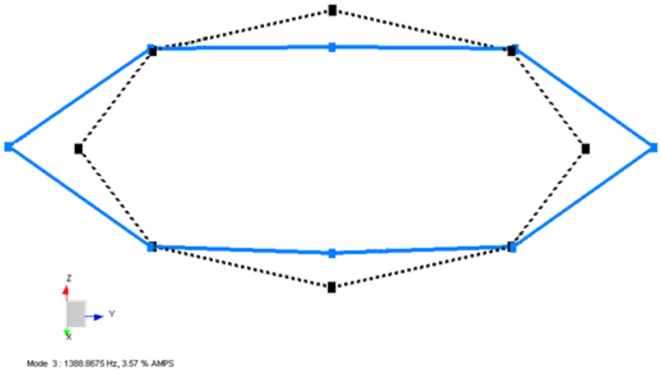

Figure 4.6 Second mode shape obtained from LMS Test Lab software for a Type-1 coil sample.

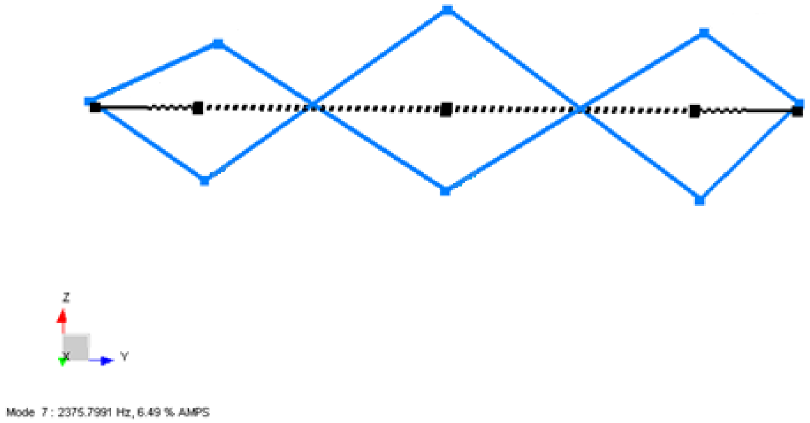

Figure 4.7 Third mode shape obtained from LMS Test Lab software for a Type-1 coil sample.

In Figure 4.5, the first bending mode of coil structure is obtained by processing both the –X and –Z excitation data. The excitation test results are merged into one complete data set to calculate the global natural frequencies and mode shapes. As expected, the first mode shape is a bending mode occurring at 789.7 Hz, as shown in Figure 4.5. The mode shape of the structure occurred bending from two points. These modes occur as twins close to each other, but not the exact same value, due to the transition zone of the quadrupole winding method, which causes the real case not to be perfectly symmetric.

In Figure 4.6, the first in-plane mode of coil structure is obtained by processing both the –X and –Z excitation data. The excitation test results are merged into one complete data set to calculate the global natural frequencies and mode shapes. As expected, the second mode shape occurred in the XY plane and it is placed at 1388.9 Hz, as shown. These modes occur as twins close to each other, but not the exact same value, due to the transition zone of the quadrupole winding method, which causes the real case not to be perfectly symmetric.

In Figure 4.7, the second out-of-plane mode of coil structure is obtained by processing both the –X and –Z excitation data. The excitation test results are merged into one complete data set to calculate the global natural frequencies and mode shapes. The third mode shape occurred as the second bending mode at 2375 Hz, as shown. The shape of the structure bends from three points. These modes occur as twins close to each other due to the transition zone of the quadrupole winding method. However, it is very difficult to monitor the three-point out-of-plane bending with four moving accelerometers placed at 45-degree intervals. Luckily, in this test, the merged excitation data provides a result closer to the real situation.

The natural frequency values detected from the modal tests of the coil Type-1 are tabulated in Table 4.4.

Table 4.4 Natural frequency results from modal tests of coil Type-1

	Mode 1	**Mode 2**	**Mode 3**
Modal Test	789.34 Hz	1389.48 Hz	2374.85 Hz

The mode shapes and resonance frequencies found for the Type-1 coil batch from the modal tests are compared with the RVE-based global FE model for the Type-1 coil configuration. If they are compatible, the geometry of the FE model is set to a Type-2 coil configuration and tested with the same procedure as stated in Section 3.3 to verify the RVE-based FE model by taking the material properties and the previously calculated fixed RVE parameters.

4.3.2 Modal Test Results of Coil Type-2

The mode shapes and resonance frequencies for the Type-2 coil are discussed, and these results are compared with the RVE-based global FE model for a Type-1 configuration in Section 4.4 to verify the global FE model based on RVE method.

In the testing scheme, the axis definitions for the coil sample are: +X is the outward radial direction; and –X is the direction towards the center of the coil circle. +Z and

–Z give the out-of-plane direction when the coil is placed on the table, as shown in Figure 3.26.

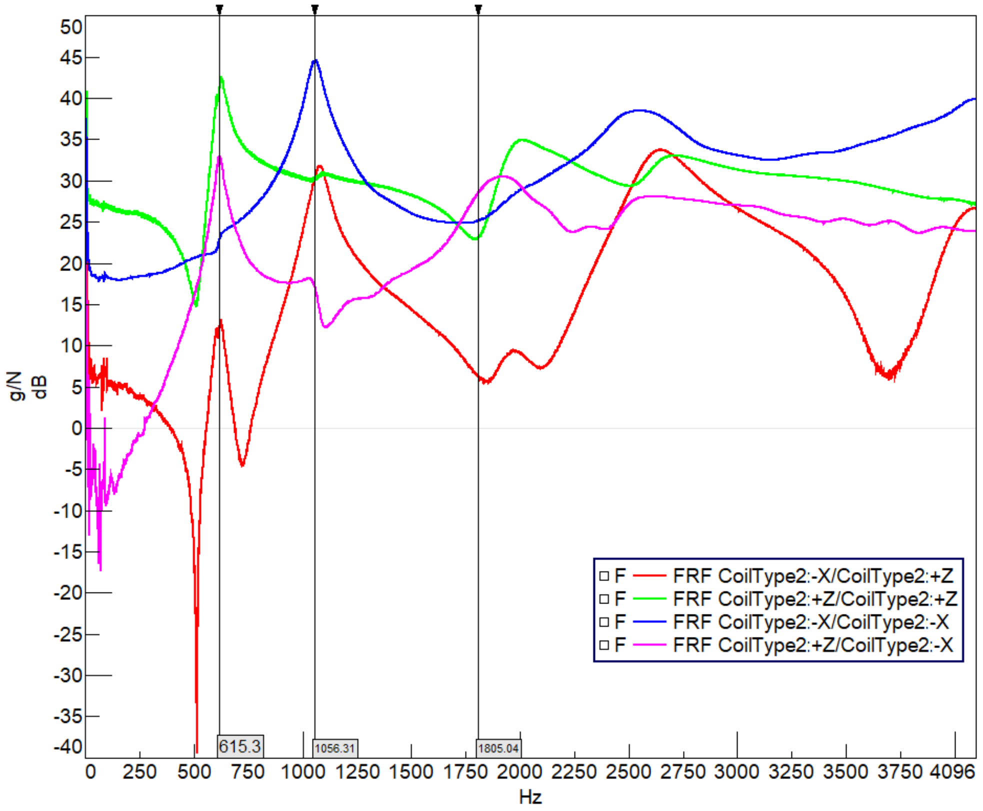

Figure 4.8 Drive point FRF for Coil Type-2.

Figure 4.8 illustrates the drive point FRF result graph for a Type-2 coil. The OX axis is frequency (Hz) and the OY axis is frequency response (g/N) shown in decibels (dB). The input from the hammer at point 1 and the response output from the accelerometer at point 1 in the –X direction (blue function) provides the modes in the radial direction mode shape frequencies as the peaks. This means the pink function shows an in-plane mode shape and a resonance movement at 1056 Hz, while the 615 Hz and 1805 Hz values show an anti-resonance. Therefore, it can be seen from the FRF that there will be a radial movement of the coil structure as the second mode, while the first and third modes are oriented in an out-of-plane (Z) direction. In addition, the green line is the FRF curve for the out-of-plane (Z) excitation and response. The main peak point for the structure occurs at the 615 Hz and 1805 Hz values as the first and third modes, so the out-of-plane bending modes are located at these frequencies [66].

In Figures 4.9–4.11, the orange lines represent the deformed shape, while the black dashed lines represent the undeformed shape of the Type-2 coil.

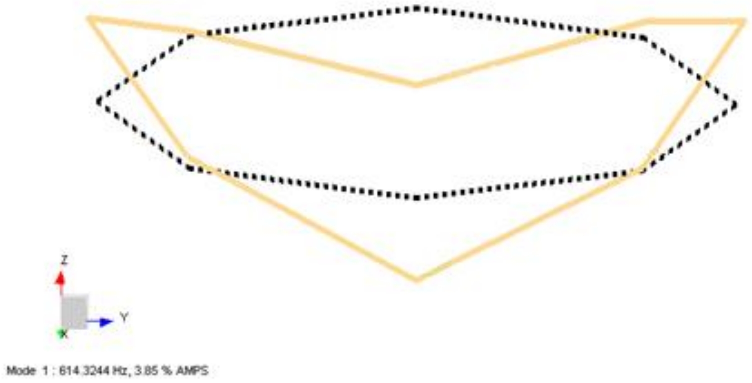

Figure 4.9 First mode shape obtained from LMS Test Lab software for the Type-2 coil sample.

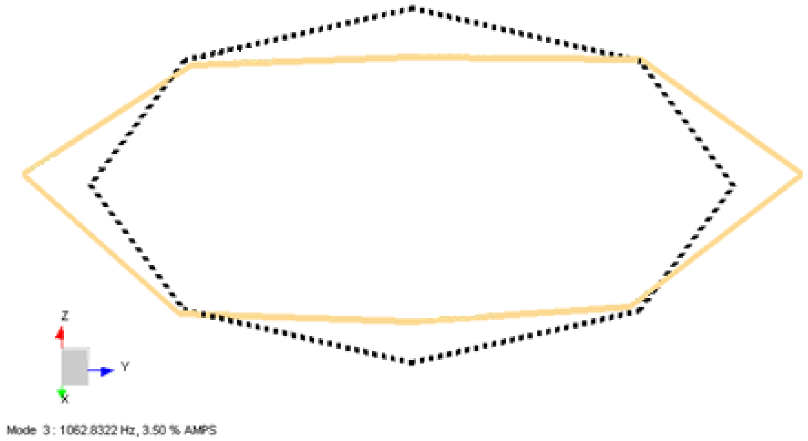

Figure 4.10 Second mode shape obtained from LMS Test Lab software for the Type-2 coil sample.

Figure 4.11 Third mode shape obtained from LMS Test Lab software for the Type-2 coil sample.

In Figure 4.9, the first bending mode of coil structure is obtained by processing both the –X and –Z excitation data merged. As expected, the first mode shape is a bending mode and it occurs at 614 Hz, as shown. The shape of the structure bends from two points, similar to the results in Figure 4.5.

In Figure 4.10, the first in-plane mode of coil structure is obtained by processing both the –X and –Z excitation data merged. As expected, the second mode shape occurs in the XY plane at 1062 Hz, as shown. The coil shows the same behavior compared with Figure 4.6, as expected.

In Figure 4.11, the second out-of-plane mode of coil structure is obtained by processing both the –X and –Z excitation data. The excitation test results are merged into one complete data set to calculate the global natural frequencies and mode shapes. The third mode shape occurs as the second bending mode at 1937 Hz, as shown. The shape of the structure bends from three points. These modes occur as twins close to each other due to the transition zone of the quadrupole winding method. However, it is very difficult to monitor the three-point out-of-plane bending with four moving accelerometers placed at 45-degree intervals. In this test, the merged excitation data does not give a natural frequency result close to the real situation. In this study, we are interested in the first two modes, eliminating their effects on sensor performance so the exact values are not a serious concern for the third mode.

The natural frequency values detected from the modal tests of the coil Type-2 are tabulated in Table 4.5.

Table 4.5 Natural frequency results from modal tests of coil Type-2

	Mode 1	**Mode 2**	**Mode 3**
Modal Test	618.17 Hz	1055.54 Hz	1814.25 Hz

The results found for each coil case are expected for a ring-shaped structure in which an out-of-plane mode occurs prior to the in-plane mode. Because of the elastic modulus of the glass fiber part being higher than the elastic modulus of adhesive part, the circumferential stiffness should be higher compared with the axial direction, and the collected results for both coil configurations in modal testing processes give a meaningful order for the mode shapes for a ring-shaped coil structure.

4.4 Comparison of Analysis and Test Results

The average results of the modal tests for the produced Type-1 coil sets, which contain five coil samples, and the modal analysis results for the same coil in the finite element model are compared in Table 4.6. The percent error gives the percentage between the FE modal analysis and the modal test. The standard deviation values for the modal test natural frequencies of the five coils are 2.1%, 0.8%, and 2.9%, respectively, for mode 1, mode 2, and mode 3 for Type-1 coil fiber winding.

Table 4.6 Comparison of test and analysis results for the coil Type-1.

	Mode 1	**Mode 2**	**Mode 3**
Modal Test	789.34 Hz	1389.48 Hz	2374.85 Hz
Modal Analysis	761.62 Hz	1535.9 Hz	2328.5 Hz
Percent Error	3.51%	10.53%	1.95%

In Table 4.6, it can be seen that the first mode, which is the first out-of-plane movement, is approximated with an error below 4%. The second mode, which represents in-plane movements, is approximated at around a 10% error gap. In this global FE model, the jogging zone of the fibers are not modeled. The coil is assumed to be perfectly symmetric, which was not the real situation. The approximation of the first natural frequency is the most crucial one for the designer to shape the coil support for the coil geometry. This result says to the designer that the first mode shape dynamics in the coil are modeled with a correct approach compared with the real coil situation.

The average results of the modal tests for the produced Type-2 coil sets, which contain five coil samples, and the modal analysis results for the same coil in the finite element model are compared in Table 4.7. The standard deviation values for the modal test natural frequencies of five coils are 1.5%, 0.9%, and 2.7%, respectively, for mode 1, mode 2, and mode 3 for Type-2 coil fiber winding.

Table 4.7 Comparison of test and analysis results for the coil Type-2.

	Mode 1	**Mode 2**	**Mode 3**
Modal Test	618.17 Hz	1055.54 Hz	1814.25 Hz
Modal Analysis	604.82 Hz	1173.1 Hz	2071.2 Hz
Percent Error	2.21%	10.02%	12.41%

It can be seen from Table 4.7 that the first mode, which is an out-of-plane movement, is approximated with an error nearly 2%. The second mode, which represents in-plane movements, is approximated at around a 10% error gap.

For the modeling, the finite element (FE) method is used to construct a model based on the representative volume element in which the global parameters determined. The global model results of the FE model for Type-1 coil are then compared with the impact modal test results. Next, the Type-2 coil global FE model is constructed with the same homogenized RVE parameters and compared with the modal test results. The first natural frequencies of both structures are approximated with almost 3% error compared with the produced coil configurations.

CHAPTER 5

DISCUSSION AND CONCLUSION

In this study, the dynamic behaviors of fiber-optic gyroscopes (FOGs) are studied through a multiscale modeling approach in comparison with experimental observations. Initially, a representative volume element is generated to obtain the macroscopic material parameters, including the influence of microstructure through a step-by-step approach with proper boundary conditions. The obtained parameters are used for the orthotropic material model, which are employed for the modal analysis of the FOG coil in ABAQUS software. The results are compared with the experimental findings and, after obtaining a satisfactory agreement, the approach is successfully applied for another FOG coil with a different fiber length, to increase the reliability of using such an approach for the analysis of FOGs in general. In this approach, a maximum error of below 12% between the results of FE modeling and modal tests is achieved. Moreover, the first natural frequencies of the structures are provided with an error less than 3%. Owing to this work, fiber-optic coils with different fiber lengths can be identified by means of the dynamic behavior for the estimation of coil support types and their effects on sensor performance. Pre-known coil mode shapes and their frequencies provide information to the designer on whether they need to focus on a vibration based error or not, even if the coil is not produced or tested at all. Therefore, the performance grade of the fiber-optic coil could be enhanced according to the needs of the platform.

In order to solve the complex orthotropic material behavior issue of the FOG coil, RVE-based multiscale analysis methodology is employed and the vibrational properties of multiscale FOG coils are obtained from both experimental modal analysis and finite element calculations. The novelty of the study is in the verification of the macroscopic material properties of the FOG coil obtained from the microstructure by means of vibration tests. Studies regarding the vibrational properties of composite materials are uncommon and, especially with regard to fiber-optic gyro sensors, an experimental modal analysis approach is rare in the literature. By using this procedure, more robust FOG designs can be achieved in the context of vibration problems.

An important and valuable result of this study is that the dynamic behavior and support structure design requirements for FOG coils can be estimated and decisions can be made prior to the manufacturing and testing stages. Production and prototype testing costs may be reduced, or even totally avoided, with such global FE models for different geometric dimensions for the width or radius of coils that have different total fiber lengths. Hence, the designer can choose the available raw materials for coil supports and construct joint types between the support part and the coil part based on the geometry of the whole sensing assembly as a single complete sensing unit. The composite components of the coil and the coil support components are able to be combined in the same FE model for differing sensor grades.

The coil structure generate complications due to its orthotropic nature. A comprehensive and experimentally verified model for a FOG coil has been established as a baseline study to overcome these complications. The next stage of FOG sensor design is the simulation of the coil support together with the coil to avoid from the natural frequencies. As the coil support is mainly composed of isotropic materials, a straightforward simulation process that is less challenging can be used.

As a future work, different types of coil support designs with different geometries and raw materials can be simulated with the FE model of the FOG coil as a part of the sensor design. There are mainly two types of sensor supports with respect to the general geometrical shape. The first one is represented by the letter "C" and one side of the support is flange while the other side of the coil is set free. This tray type of support geometry is advantageous in terms of thermal loadings such that one side is free to expand in the width of the coil without creating mechanical stresses. The second support type is represented by the letter "H" that two sides of the coil is covered with the support and coil is constricted. The structure is more stiff similar to the I-beams and the resonant frequencies occurs at higher values. They both have advantages and disadvantages over each other. However, with the help of the developing technology, some futuristic raw materials can be employed by using innovative methods of production. In support components, 3D printed CFRP, Glass Fibers or composite structures can be used. The support geometries can also be used as functioning both like a winding mandrel and limiting mandrel by implementing compatible composite material usage. One set of mandrels is used for every a few coil production. By designing the coil support functioning like a mandrel, the usage and disposal of the set of mandrels can be eliminated.

REFERENCES

[1] Lefèvre, H. The Fiber-Optic Gyroscope, 2nd edition; Artech House: Norwood: MA, USA, 2014.

[2] Barbour, N.; Schmidt, G. Inertial sensor technology trends. IEEE Sensors Journal, 2001, 1, 332–339.

[3] Kumagai, T.; Soekawa, H.; Yuhara, T.; Kajioka, H.; Oho, S.; Sonobe, H. Fiber optic gyroscopes for vehicle navigation systems. In Proceedings of the SPIE Vol. 2070, Fiber Optic and Laser Sensors XI, Boston, MA, USA, 1994.

[4] Lad, P.B. Design and Evaluation of an Automated Fiber Optic Untwisting Machine. Ph.D. Thesis, Massachusetts Institute of Technology, Cambridge, MA, USA, 1999.

[5] Seçmen, B. Simulation on Interferometric Fiber Optic Gyroscope with Amplified Optical Feedback. Ph.D. Thesis, Middle East Technical University, Ankara, Turkey, 2003.

[6] Alaçakır, E. Modeling of Environmental Temperature Dependency for Sensors Operated by Sagnac Effect. MSc. Thesis, Middle East Technical University, Ankara, Turkey, 2019.

[7] Armenise, M. N.; Ciminelli, C.; Dell'Olio, F.; Passaro, V. M. N., Advances in gyroscope technologies. ISBN 10: Springer Science and Business Media, 2014.

[8] Passaro, V. M., Cuccovillo, A., Vaiani, L., Carlo, M. D., & Campanella, C. E. Gyroscope Technology and Applications: A Review in the Industrial Perspective. Sensors, 17(10), 2284, 2017.

[9] Groves, P. D. Principle of GNSS, Inertial and Multisensor Integrated Navigation Systems, 2nd Edition. Boston: Artect House, 2013.

[10] Woodman, O. J. An Introduction to Inertial Navigation. Strapdown Inertial Navigation Technology, 1-37, 2007.

[11] Titterton, D.; Weston, J. Strapdown Inertial Navigation Technology; Institution of Engineering and Technology: Stevenage, UK, 2004.

[12] Heimann, M.; Liesegang, M.; Arndt-Staufenbiel, N.; Schröder, H.; Lang, K.-D. Optical system components for navigation grade fiber optic gyroscopes. In Proceedings of the SPIE Vol. 8899, Emerging Technologies in Security and Defence and Quantum Security II; and Unmanned Sensor Systems X, Dresden, Germany, 2013.

[13] Juang, J.N.; Radharamanan, R. Evaluation of Ring Laser and Fiber Optic Gyroscope Technology; Mercer University: Macon, GA, USA, 2009.

[14] Ruffin, P.B. A review of fiber optics technology for military applications. In Proceedings of the SPIE Vol. 10299, Novel Materials and Crystal Growth Techniques for Nonlinear Optical Devices: A Critical Review, San Jose, CA, USA, 2000.

[15] Nayak, J. Fiber-optic gyroscopes: From design to production [Invited]. OSA Publishing Group, Applied Optics, Vol. 50, Issue 25, 2011.

[16] Shupe, D. M. Thermally induced nonreciprocity in the fiber-optic interferometer. Applied Optics, 1980, 19, 654–655.

[17] Frigo, N.J. Compensation of linear sources of non-reciprocity in sagnac interferometers. In Proceedings of the SPIE Vol. 0412, Fiber Optic and Laser Sensors I, Arlington, TX, USA, 1983.

[18] Li, M.; Liu, T.; Zhou, Y.; Jiang, J.; Hou, L.; Wang, J.; Yao, X. S. A 3d model for analyzing thermal transient effects in fiber gyro coils. In Proceedings of the SPIE Vol. 6830, Advanced Sensor Systems and Applications III, Beijing, China, 2008.

[19] Ling, W.; Li, X.; Yang, H.; Liu, P.; Xu, Z.; Wei, Y. Reduction of the shupe effect in interferometric fiber optic gyroscopes: The double cylinder-wound coil. Optics Communications, 2016, 370, 62–67.

[20] Li, X.; Ling, W.; He, K.; Xu, Z.; Du, S. A thermal performance analysis and comparison of fiber coils with the d-cylwinding and qad winding methods. Sensors 2016, 16, 900.

[21] Varnham, M.P.; Payne, D.N.; Barlow, A.J.; Birch, R.D. Analytic solution for the birefringence produced by thermal stress in polarization maintaining optical fibers. IEEE, Journal of Lightwave Technology, 1983, 1, 332–339.

[22] Choi, W.S. Analysis of temperature dependence of thermally induced transient effect in interferometric fiber-optic gyroscopes. Journal of Optical Society of Korea 2011, 15, 237–243.

[23] Li, Z.; Meng, Z.; Liu, T.; Yao, X.S. A novel method for determining and improving the quality of a quadrupolar fiber gyro coil under temperature variations. Optics Express 2013, 21, 2521–2530.

[24] Zhang, Z.; Yu, F. Quantitative analysis for the effect of the thermal physical property parameter of adhesive on the thermal performance of the quadrupolar fiber coil. Optics Express 2017, 25, 30513.

[25] Zheng, Z.; Wang, Y.; Yu, J.; Liu, B.; Li, M.; Chen, G. Full—Parameters mathematical model of high precision fiber optic gyroscope coil and automatic forming technology. In Proceedings of the 2020 IEEE International Symposium on Inertial Sensors and Systems (INERTIAL), Hiroshima, Japan, 2020.

[26] Tirat, O.F.; Euverte, J.M. Finite element model of thermal transient effect in fiber optic gyro. In Proceedings of the SPIE Vol. 2837, Fiber Optic Gyros: 20th Anniversary Conference, Denver, CO, USA, 1996.

[27] Minakuchi, S.; Sanada, T.; Takeda, N.; Mitani, S.; Mizutani, T.; Sasaki, Y.; Shinozaki, K. Thermal strain in lightweight composite fiber-optic gyroscope for space application. Journal of Lightwave Technology, 2015, 33, 2658–2662.

[28] Ogut, S.; Osunluk, B.; Ozbay, E. Modeling of thermal sensitivity of a fiber optic gyroscope coil with practical quadrupole winding. In Proceedings of the SPIE Vol. 10208, Fiber Optic Sensors and Applications XIV, Anaheim, CA, USA, 27 April 2017.

[29] Osunluk, B.; Ogut, S.; Ozbay, E. Thermally induced bias error due to strain inhomogeneity through the fiber optic gyroscope coil. Applied Optics, 2017, 59, 10416–10421.

[30] Osunluk, B.; Ogut, S.; Ozbay, E. Reduction of thermal strain induced rate error for navigation grade fiber optic gyroscope. In Proceedings of the DGON Inertial Sensors and Systems 2018, Braunschweig, Germany, 24–28 September 2018.

[31] Tantaswadi, P. Numerical Analysis of Current Measurement Error Due to Vibration in Reciprocal Fiber-Optic Polarimetric Current Sensor Thammasat International Journal of Science and Technology, Vol.8, No.l, 2003.

[32] Jia, M.; Yang, G. Research of optical fiber coil winding model based on large-deformation theory of elasticity and its application. Chinese Journal of Aeronautics, 2011, 24, 640–647.

[33] Shan, L.; Li, J.; Liu, J.; Su, H.; Liang, Y. Low strain variation design method of the quadrupolar fiber coil based on the comprehensive stress analysis. Optoelectronics and Advance Materials, Rapid Communications, 2017, 11, 342–348.

[34] Gao, Z.; Zhang, Y.; Zhang, Y. Modeling for IFOG vibration error based on the strain distribution of quadrupolar fiber coil. Sensors 2016, 16, 1131.

[35] Yang, D.S. Design of fiber optic gyro inertial measurement system with high vibration resistance. In Proceedings of the 2nd International Conference on Electrical and Electronic Engineering, Hangzhou, China, 26–27 May 2019.

[36] Song, R.; Chen, X. Analysis of fiber optic gyroscope vibration error based on improved local mean decomposition and kernel principal component analysis. Applied Optics, 2017, 56, 2265.

[37] Song, N.; Zhang, C.; Du, X. Analysis of vibration error in fiber optic gyroscope. In Proceedings of the SPIE Vol. 4920, Advanced Sensor Systems and Applications, Shanghai, China, 2002.

[38] Wu, L.; Cheng, J.; Sun, F. Research on anti–vibration scheme of FOG SINS. In Proceedings of 2009 the International Conference on Computer Engineering and Technology, Washington, DC, USA, Vol. 2, 22–24 January 2009.

[39] Ma, Y.; Quan, B.; Han, Z.; Wang, J. Structural optimization of the path length control mirror for ring laser gyro. In Proceedings of the SPIE Vol. 10256, Second International Conference on Photonics and Optical Engineering, Xi’an, China, 28 February 2017

[40] Fenercioğlu, T.O.; Yalçinkaya, T. Design optimization of a laser path length controller through numerical analysis and experimental validation. International Journal of Applied Electromagnetics and Mechanics, 2019, 61, 429–443.

[41] Fenercioğlu, T.O.; Yalçinkaya, T. Computational-experimental design framework for laser path length controller. Sensors 2021, 21, 5209.

[42] Liu, X.; Jin, B.; Bai, Q.; Wang, Y.; Wang, D. and Wang, Y. Distributed Fiber-Optic Sensors for Vibration Detection. Sensors 2016, 16, 1164.

[43] Zhoumin, Z.; Wenbin, H.; Fang, L.; Weibing, G; Yan, Y. Vibration error research of fiber optic gyroscope in engineering surveying. Telkomnika Vol. 11, No. 4, pp. 1948~1955, 2013.

[44] Yalçinkaya, T.; Çakmak, S.O.; Tekoğlu, C. A crystal plasticity based finite element framework for RVE calculations of two-phase materials: Void nucleation in dual-phase steels. Finite Element in Analysis and Design, 2021, 187, 103510.

[45] Yalçinkaya, T.; Gungor, G.O.; Cakmak, S.O.; Tekoğlu, C. A micromechanics based numerical investigation of dual phase steels. Procedia Structural Integrity, 2019, 21, 61–72.

[46] Acar, S.S.; Bulut, O.; Yalçinkaya, T. Crystal plasticity modeling of additively manufactured metallic microstructures. Procedia Structural Integrity, 2022, 35, 219-227.

[47] Bulut, O.; Acar, S.S.; Yalçinkaya, T. The influence of thickness/grain size ratio in microforming through crystal plasticity. Procedia Structural Integrity, 2022, 35, 228-236.

[48] Chen, J.; Ding, N.; Li, Z.; Wang, W. Enhanced environmental performance of fiber optic gyroscope by an adhesive potting technology. Applied Optics, 2015, 54, 7828.

[49] Gillooly, A.; Hill, M.; Read, T.; Maton, P. Next generation optical fibers for small diameter fiber optic Gyroscope (FOG) coils. In Proceedings of the 2017 DGON Inertial Sensors and Systems, Karlsruhe, Germany, 19–20 September 2017.

[50] Andreassen, E.; Andreasen, C.S. How to determine composite material properties using numerical homogenization. Computational Material Science, 2014, 83, 488–495.

[51] Barbero, E. Finite Element Analysis of Composite Materials Using Abaqus™; CRC Press: Boca Raton, FL, USA, 2013.

[52] Barbero, E. Introduction to Composite Materials Design, 3rd ed.; CRC Press: Boca Raton, FL, USA, 2018.

[53] El Moumen, A.; Tarfaoui, M.; Lafdi, K. Computational homogenization of mechanical properties for laminate composites reinforced with thin film made of carbon nanotubes. Applied Composite Materials, 2018, 25, 569–588.

[54] Jiang, W. G.; Zhong, R. Z.; Qin, Q. H.; Tong, Y. G.; Homogenized finite element analysis on effective elastoplastic mechanical behaviors of composite with imperfect interfaces. International Journal of Molecular Sciences, 2014, 15, 23389–23407.

[55] Medeiros, R.; Moreno, M.; Marques, F.; Tita, V. Effective properties evaluation for smart composite materials. Journal of the Brazilian Society of Mechanical Sciences and Engineering, 2012, 34, 362–370.

[56] Otero, F.; Oller, S.; Martinez, X.; Salomon, O. Numerical homogenization for composite materials analysis. comparison with other micro mechanical formulations. Composite Structures, 2015, 122, 405–416.

[57] Yu, W.; Tang, T. Variational asymptotic method for unit cell homogenization of periodically heterogeneous materials. International Journal of Solids and Structures, 2007, 44, 3738–3755.

[58] Gürses, K.; Kuran, B.; Gençoğlu, C. Identification of material properties of composite plates utilizing model updating and response surface techniques. In Proceedings of the International Modal Analysis Conference XXIX, Jacksonville, FL, USA, 12 February 2011.

[59] Maia, N.; Silva, J. Theoretical and Experimental Modal Analysis; Research Studies Press: Boston, MA, USA, 1997.

[60] Ewins, D.J. Modal Testing: Theory, Practice, and Application; 2nd edition; Research Studies Press: Boston, MA, USA, 2000.

[61] Avitable, P. Experimental Modal Analysis a Simple Non-Mathematical Presentation. University of Massachusetts Lowell, Lowell, Massachusetts, Sound and Vibration, 2001.

[62] Fang, Z.; Chin, K. K.; Qu, R.; Cai, H. Fundamentals of optical fiber sensors. John Wiley and Sons, 2012.

[63] Zhang, Y.; Gao, Z. Fiber optic gyroscope vibration error due to fiber tail length asymmetry based on elastic-optic effect. SPIE Vol. 51(12), 124403, Optical Engineering, 2012.

[64] Gençoğlu, C. Active vibration control of beams and cylindrical structures using piezoelectric patches. MSc. Thesis, Middle East Technical University, Ankara, Turkey, 2014.

[65] ABAQUS. Abaqus Documentation, version 2020; Dassault Systémes: Providence, RI, USA, 20.

[66] Kahveci, Ö.; Gençoğlu, C.; Yalçınkaya, T. Experimental Analysis and Multiscale Modeling of the Dynamics of a Fiber-Optic Coil. Sensors 2022, 22, 582.